Hidden Vibronic and Excitonic Structure and Vibronic Coherence Transfer in the Bacterial Reaction Center

Veronica R. Policht^{1†}, Andrew Niedringhaus¹, Rhiannon Willow¹, Philip D. Laible², David F. Bocian³, Christine Kirmaier⁴, Dewey Holten⁴, Tomáš Mančal⁵, and Jennifer P. Ogilvie^{1*}

Abstract

We report two-dimensional electronic spectroscopy experiments on the bacterial reaction center (BRC) from purple bacteria, revealing hidden vibronic and excitonic structure. Through analysis of the coherent dynamics of the BRC we identify multiple quasi-resonances between pigment vibrations and excitonic energy gaps, and vibronic coherence transfer processes that are typically neglected in standard models of photosynthetic energy transfer and charge separation. We support our assignment with control experiments on bacteriochlorophyll and simulations of the coherent dynamics using a reduced excitonic model of the BRC. We find that specific vibronic coherence processes can readily reveal weak exciton transitions. While the functional relevance of such processes is unclear, they provide a spectroscopic tool that utilizes vibrations as a window for observing excited state structure and dynamics elsewhere in the BRC via vibronic coupling. Vibronic coherence transfer clearly reveals the upper exciton of the "special pair" that was weakly visible in previous 2DES experiments.

Teaser

Coherent oscillations reveal weak electronic structure and vibronic coherence transfer in photosynthetic pigment-protein complexes.

¹Department of Physics, University of Michigan, 450 Church St, Ann Arbor MI 48109.

²Biosciences Division, Argonne National Laboratory, Argonne, IL 60439, USA.

³Department of Chemistry, University of California, Riverside, CA 92521, USA.

⁴Department of Chemistry, Washington University, St. Louis, MO 63130, USA.

⁵Faculty of Mathematics and Physics, Charles University, Ke Karlovu 5, CZ-12116 Prague 2, Czech Republic.

[†]Present address: Politecnico di Milano, Department of Physics, 20133 Milan, Italy.

^{*}e-mail: jogilvie@umich.edu

MAIN TEXT

Introduction

In the primary steps of photosynthesis, light-harvesting antenna structures gather solar energy and transfer it to reaction centers (RCs) for processing(*I*). Compared to the colorful array of photosynthetic antenna architectures that exist in nature, the RC structures are more widely conserved. The bacterial RC (BRC) from purple bacteria(*2*) features a pseudo two-fold-symmetric hexameric core of pigments (Fig. 1A) that converts excitation energy to a stable charge-separated state. The near unity quantum efficiency of the charge separation process is remarkable(*2*, *3*), as is the high specificity with which charge separation occurs along the "A" branch of the BRC structure(*2*, *4*). In contrast to the Photosystem I and Photosystem II RCs in oxygenic photosynthesis, the BRC possesses a strongly coupled "special pair" of bacteriochlorophyll a (BChl), yielding greater spectral separation between the absorption features in the Q_y region (Fig. 1B) making the BRC a simpler system for resolving the ultrafast processes of energy transfer and charge separation(*5*). Understanding the design principles of photosynthetic systems may open new avenues for improving artificial solar harvesting devices and has helped motivate the development of new subfields of spectroscopy and theoretical approaches to describing the nonequilibrium photosynthetic process.

The combination of ultrafast timescales (~fs - ps) on which photosynthetic systems perform energy transfer and charge separation, and their broad absorptions arising from multiple coupled pigments in carefully-tuned dielectric environments present significant challenges to uncovering their structure-function relationship. Two-dimensional electronic spectroscopy (2DES) can address many of these challenges and has become a powerful tool for studying photosynthetic systems (6– 9). 2DES studies of the Fenna-Matthews-Olson (FMO) complex demonstrated its ability to uncover energy transfer pathways(6) and revealed long-lived (\sim ps) coherent oscillations(10),(11). Similar coherent processes have been reported in other photosynthetic systems(8). Ultrafast pump probe studies of the BRC by Vos and Martin(12, 13) in the early '90s provided the first observations of coherent dynamics in photosynthetic systems. These studies proposed that the coherences arose from vibrational wave packet motion on the excited electronic state delocalized across the special pair and surrounding protein matrix(13) and might facilitate electron transfer(14). The initial 2DES experiments to observe long-lived coherences in FMO(10) proposed superpositions of delocalized electronic excited states as the origin of the coherence. The FMO study motivated theoretical work to assess the validity of the standard methods such as Redfield theory for describing the quantum dynamics of electronic energy transfer(15) and to offer alternative approaches(16–18) that could better account for coherent processes. It was later noted that the frequencies of the observed coherences matched pigment vibrational modes as well as excitonic energy gaps, raising a question about the role of vibrations in explaining both the experimental observations of coherence and the high efficiency of energy(19-22) and electron transfer(23). The prevalence of electronic-vibrational resonances and their possible functional relevance continues to be debated (14, 19, 20, 24–26). It is now understood that vibrational degrees of freedom play a dominant role in the coherent dynamics observed in 2DES studies of photosynthetic antennas(20, 27, 28) and RCs(24, 25, 29–32). Theoretical and experimental work has established how electronic, vibrational and vibronic coherence is manifest in 2DES data(7, 20, 27, 33-36). Additionally, there have been several reports of coherence transfer in molecular

systems(37–42), though determining unambiguous spectroscopic signatures of coherence transfer remains an ongoing effort.

Here we report coherence signatures from broadband 2DES studies of the neutral BRC as it undergoes energy transfer and charge separation, and compare these signatures to those obtained from monomeric BChl(43) as a control for purely vibrational coherence. The coherent dynamics reveal multiple quasi-resonances between intramolecular vibrations and electronic energy gaps identified in BRC exciton models. We find coherence signatures that cannot be explained by models of purely vibrational, electronic or vibronic coherence. Using a reduced vibronic model of the BRC we assign these signatures to specific vibronic coherence transfer processes. Coherence transfer processes are typically neglected in standard models of photosynthetic energy conversion, where vibrations are included in the spectral density rather than explicitly in the system Hamiltonian. We show that a subset of vibronic coherence transfer processes involves superposition states in which vibrations on the ground electronic state of one pigment provide a window for observing excited state dynamics elsewhere in the BRC via vibronic coupling. These processes can readily reveal weak exciton transitions, making vibronic coherence transfer a useful spectroscopic tool. In the case of the BRC it allows us to confirm our recent assignment of the upper exciton transition of the "special pair" that was only weakly visible in the 2DES correlation spectrum, and required an extensive kinetic analysis for its identification (34). While our reduced exciton model allows us to understand the origin of the coherent signals in our data, further extensive modeling that takes into account multiple vibrational modes as well as charge transfer states will be needed to draw conclusions about the functional relevance of the observed vibronic coherence transfer processes and quasi-electronic-vibrational resonances.

Detecting Coherence and Coherence Transfer in 2DES

In a 2DES experiment, a sequence of three laser pulses with inter-pulse time delays t₁ and t₂ excites the sample, inducing a third-order polarization that radiates a signal field a time t₃ after the pulse. The amplitude and phase of this signal is recorded as a function of t₁ and t₃. A Fourier transform of the signal with respect to the t₁ and t₃ delays resolves the signal along the respective "excitation" and "detection" frequency axes of the 2D spectra at a fixed "waiting time" $(t_2)(44)$. Using perturbation theory, and taking into account the experimental implementation, it is possible to enumerate all possible three-pulse interactions that contribute to the 2DES signal. These interactions can be described through so-called Liouville pathways, which chart the photo-induced time evolution of a system's density matrix represented in the basis of its eigenstates. Liouville pathways are a powerful tool for understanding the complex dynamics of a system and can be depicted using double-sided Feynman diagrams (Supplementary Fig. 1). A complete collection of the Liouville pathways and their associated signals would provide complete information about the time evolution of the system's photo-induced state; however, disentangling such a complete set from experimental data is usually not feasible. Here we focus on the subset of pathways that give rise to coherent oscillatory signals during waiting time, t2. Such pathways originate from coherence between two eigenstates of the system, which produce beating signals at the characteristic frequency corresponding to the difference between the eigenstate energies. These beating signals can be selectively revealed by a Fourier transform with respect to the waiting time, t_2 . The 2D distribution of beating signals at conjugate frequency ω_2 , referred to here as a "coherence map", provides important insight into the physical origin of the coherence by enabling assignment of specific features to different Liouville pathways(20, 24, 25, 27, 35).

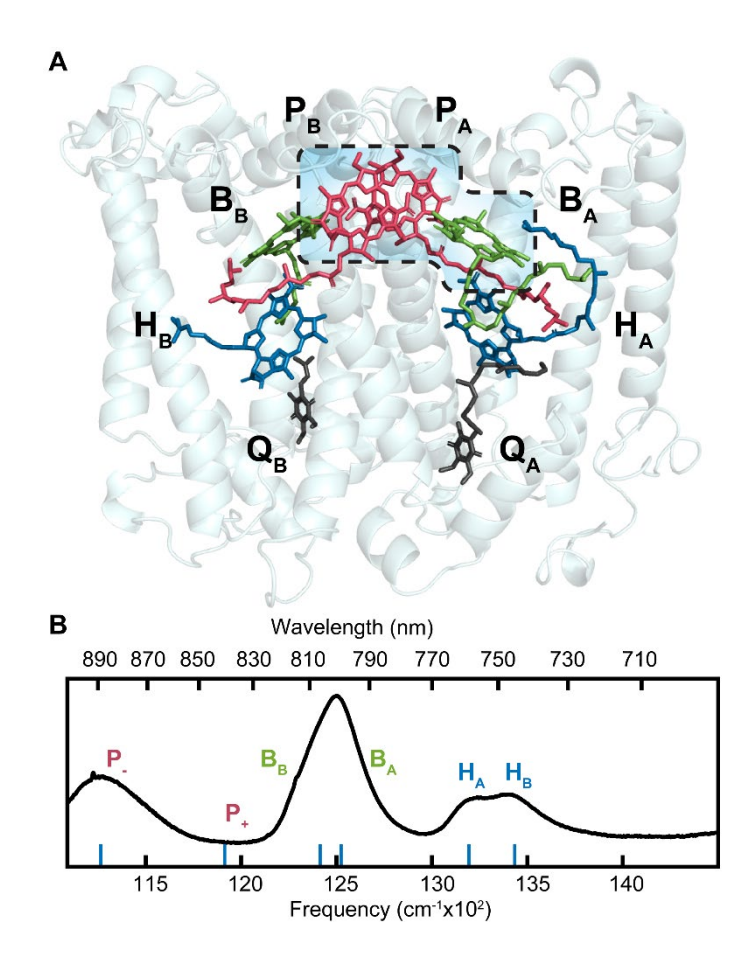


Figure 1 Spectrum and structure of the Bacterial Reaction Center. (A) Structure of the Bacterial Reaction Center of Rhodobacter sphaeroides from 2.2 Å resolution X-Ray Crystallography. Shown are two BRC protein domains, L and M, with the pigments involved in energy and charge transfer highlighted and labeled for the branches active (A) and inactive (B) during charge transfer: P - Special Pair of BChl; B – accessory BChl, H – BPheo a, Q – quinones. Rhodobacter capsulatus BRCs are thought to be structurally similar to the *Rhodobacter* sphaeroides BRC. The W(M250)V BRC mutant studied here lacks the QA molecule. Figure prepared using PyMOL with data from PDB entry 1AIJ(46). **(B)** The 77 K linear absorption spectrum for the W(M250)V BRC from Rhodobacter capsulatus is presented with excitonic peak locations, determined by Niedringhaus, et al.(50), indicated by vertical blue ticks and labels.

Results

Two-dimensional electronic spectroscopy of the BRC

We performed 2DES experiments on the W(M250)V BRC mutant of Rhodobacter capsulatus, which lacks the A side quinone (Fig. 1A) and performs charge separation to the P₊H_A- state(45). Figure 1B shows the linear absorption spectrum of the W(M250)V BRC at 77 K. Our understanding of the electronic structure of the BRC is informed by the structure as determined by X-Ray crystallography (Fig. 1A) which allows us to estimate the electronic couplings and dipole moments of the individual molecules (46, 47). The two, nearly-mirror symmetric branches of the BRC are composed of 4 BChl and two Bacteriopheophytin a (BPheo or H) molecules where the two closely-spaced and strongly-coupled BChl molecules are referred to as the special pair (P). The electronic coupling between the special pair pigments (PA, PB) is sufficiently strong that the two lowest excited states largely consist of linear combinations of excitations of PA and PB pigments and are denoted the upper (P+) and lower (P-) exciton states. Other couplings between pigment electronic transitions are relatively weak and, correspondingly, remaining electronic eigenstates of the BRC are primarily localized on the weakly-coupled BChl (B) and H pigments. Throughout this paper, we use the term exciton to refer to any electronic eigenstate of the coupled BRC. The excitons with a predominant localization on B (H) are referred to as the B (H) state or exciton. To simulate the results of the 2DES experiments, we include vibrational states explicitly on one of the pigments. Vibrational states of the pigment do not perturb the electronic structure of the BRC significantly and the eigenstates of the combined electronic-vibrational model, the socalled vibronic excitons, keep the same characteristic electronic structure, with the additional quantum number pertaining to the excitation of the vibrational mode.

Structure-based models of the BRC explain the three main peaks in the Qy linear absorption spectrum (Fig. 1A) as arising in increasing energy from the lower (P-) exciton of the special pair, the combined BChl BA and BB pigments (B), and the bacteriopheophytins HA and HB (H). In contrast, the location of P+ has been historically difficult to assign given its weak oscillator strength and proximity to the strong ~800 nm absorption of the B pigments(47). Several studies have developed excitonic models for the BRC from *Rhodobacter sphaeroides*(47–49) and *Rhodobacter* viridis(47). We previously proposed exciton energies for the Rhodobacter capsulatus BRC studied here based on a multi-excitation 2D global analysis of 2DES data by Niedringhaus et al. (50). Those energies are largely consistent with the *Rhodobacter sphaeroides* models but differ in the energy of P+. While Niedringhaus et al. noted that P+ was evident as a weak cross-peak in the 2DES correlation spectrum (at $t_2 = 0$), a multi-excitation global analysis of the population kinetics assisted in the assignment of the P+ state(50). This previous study focused on resolving the charge separation mechanism of the M(250)V BRC using hyperbolically sampled data spanning waiting times of fs to ns. In this present study we focus on the coherent oscillatory signals as observed using even 10-fs t₂ time steps out to 3.5 ps in order to accurately resolve coherent oscillations with a 9.8 cm⁻¹ frequency resolution up to a maximum frequency of 1680 cm⁻¹. As a control for purely vibrational coherence effects, we also present 2DES data of monomeric BChl (Supplementary Fig. 2)(43).

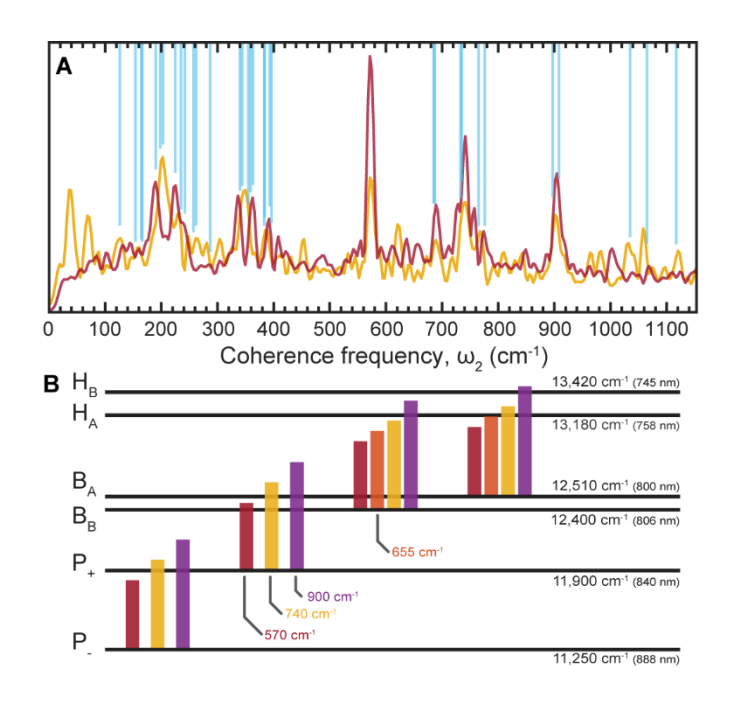


Figure 2(A) Frobenius spectra for the W(M250)V BRC (red) and bacteriochlorophyll a (gold). Blue lines indicate vibrational modes of BChl and Bacteriopheophytin a(51-53) that lie within the experimental resolution (9.7 cm⁻¹) of the most prominent peaks in the Frobenius spectra. Peak prominence is determined by ≥15% of the Frobenius spectrum maximum above the background noise level. It is worth noting that the BRC Frobenius spectrum is largely dominated by B-band contributions. Several less-prominent modes not highlighted here are also in good agreement with vibrational modes such as the ω_2 = 656 cm⁻¹ mode (Supplementary Fig. 3). (**B**) The excitonic levels with energies taken from Niedringhaus et al.(50) demonstrates how several prominent coherence modes are in quasi-resonance with the energetic gap between excitonic levels.

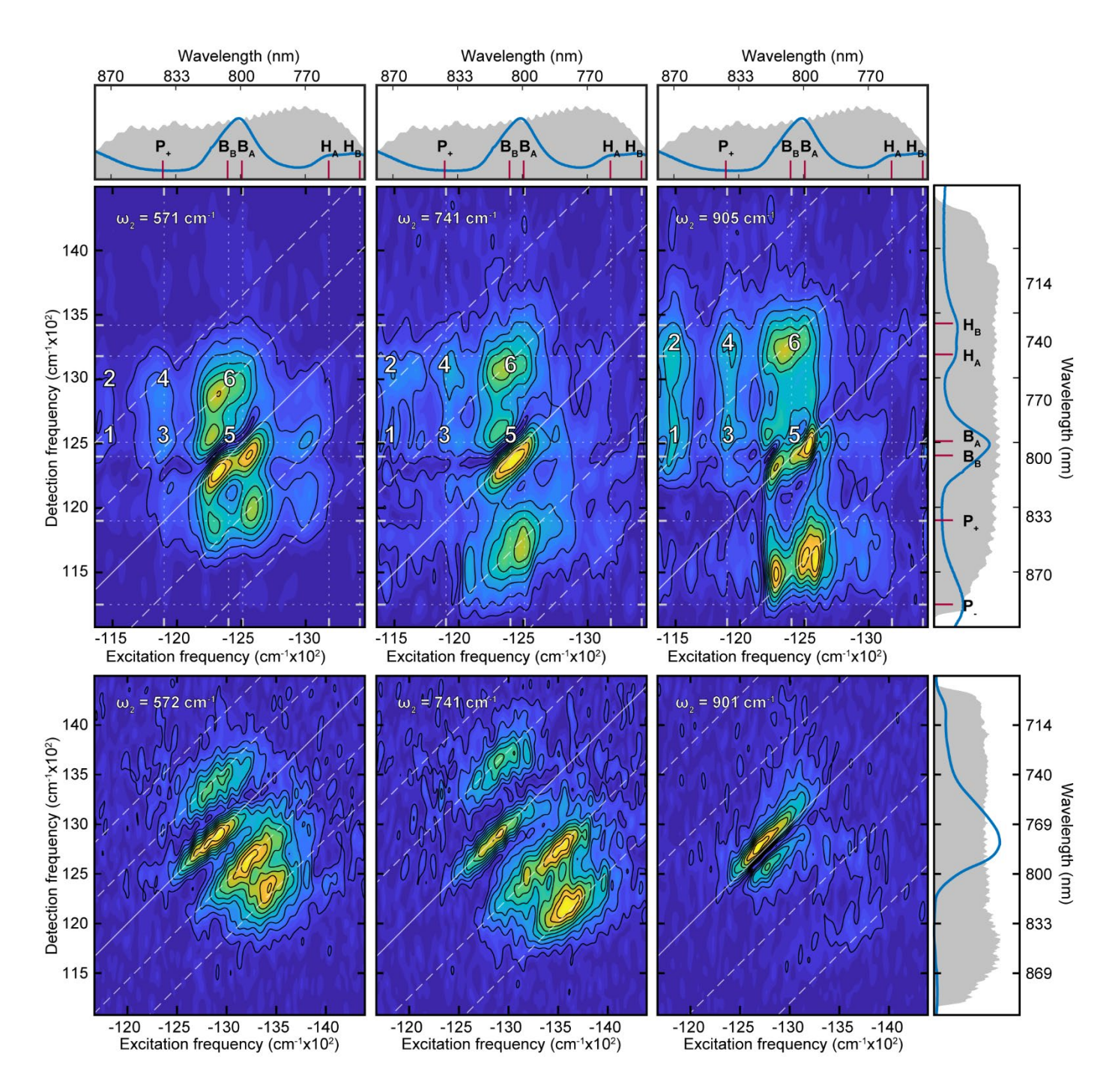


Figure 3 Coherence amplitude maps. Coherence maps of the BRC (top row) and monomeric BChl (bottom row) reveal the distribution of the observed coherent dynamics throughout the 2D spectra. Maps are derived from the real rephasing 2D spectra at ω_2 values of 572 cm⁻¹, 741 cm⁻¹ and 905 cm⁻¹ (columns left to right). For each map, the diagonal ($\omega_{\text{exc}} = \omega_{\text{det}}$) is indicated by a solid diagonal line and parallel dashed white lines are offset from the diagonal by $\pm \omega_2$ and $-2\omega_2$ to aid in their interpretation. (Top row) BRC excitonic energies taken from Niedringhaus, et.al.(50) are indicated by white dotted vertical and horizontal lines. The 77K linear absorption spectrum and probe spectra are shown for easy reference for both BRC and BChl; we additionally show the pump spectrum for the BRC maps. (Top row) Signatures labeled 1-6 show evidence for vibronic coupling between the P+, P- and BA states and are discussed in more detail in the text.

Excitonic and Vibronic Structure in the BRC

We analyze the coherent dynamics in our 2DES data by first fitting and subtracting the population kinetics, followed by Fourier transformation of the oscillatory residual with respect to t₂. To reveal the dominant coherence frequencies that are present in the 2D spectrum during t2, we take the "Frobenius norm", which sums over excitation (ω_{exc}) and detection frequency axes (ω_{det}) (Fig. 2A, red curve). For comparison we also show the Frobenius spectrum of BChl in isopropanol (gold curve)(43). Above the Frobenius spectra we indicate vibrational modes reported in resonance Raman experiments of BChl(51-53) and BPheo(53) which show good agreement with the peak positions of the Frobenius spectra. The prominent coherence modes in the Frobenius spectrum of the BRC correspond well with those reported in previous studies of coherence in the BRC(29-32) and also show good agreement with coherences reported in previous studies of BChl(33, 40–42). The similarity between the BRC peak frequencies and the modes found in the Frobenius spectrum of monomeric BChl and the vibrational spectroscopy literature for BChl monomers (51-53) is consistent with a strong vibrational character of the BRC coherences. We note a substantial discrepancy in the low frequency region of the Frobenius spectra where the single peaks in the monomer spectrum at ~200 cm⁻¹ and ~340 cm⁻¹ appear split into two neighboring peaks in the BRC spectrum. This splitting of the low-frequency peaks is consistent with peak frequency shifts observed in resonance Raman experiments which selectively excited either the P- or B bands(51, 54).

Figure 2B shows the ladder of excitonic states of the BRC determined by Niedringhaus et al(50). Superimposed on the excitonic ladder we show the dominant coherent modes from the Frobenius spectrum of Fig 2A, drawn with height to scale with respect to the excitonic energy gaps. It is evident from Fig. 2B that there are numerous coherent modes in quasi-resonance with excitonic energy gaps in the BRC, with an energy mismatch of tens of wavenumbers. Given that the vibrational spectra of bacteriochlorins are very dense, it is not surprising that there exist vibrational modes close to resonance with the excitonic energy gaps of the BRC. The interaction of electronic and vibrational degrees of freedom has been shown to lead to vibronic delocalization and modification of the allowedness of otherwise forbidden transitions(20–22, 27).

To gain insight into the physical origin of the coherent processes in the BRC we examine coherence maps, which display the 2D amplitude distribution at individual coherence frequencies (Fig. 3). These coherence maps are obtained by plotting, at a given ω_2 , the absolute magnitude of the FFT of the oscillatory residual (after subtraction of the population kinetics) to each ($\omega_{\rm exc}$, $\omega_{\rm det}$) point of the real rephasing 2D spectrum(28, 34). By displaying the excitation and detection frequency dependence of the coherence amplitude we can more easily assign specific peaks to particular Liouville pathways (see Supplementary Fig. 7 & 8). Further details of the coherence analysis are provided in the Supplementary Materials.

Whereas the Frobenius spectra of the BRC and BChl monomer show very good agreement above ~200 cm⁻¹, clear differences between the coherence maps of the BRC and BChl monomer (Fig. 3) emerge due to the vibronic structure of the BRC. Figure 3 shows coherence maps for modes in quasi-resonance with excitonic energy gaps as identified in the Frobenius spectrum (Fig. 2A). Additional coherence maps are presented in the Supplementary Material. The BRC coherence maps show numerous peaks, with the strongest centered around the B transition (labeled 5 & 6). By comparing the coherence peak distribution of the signals centered around B with the BChl

monomer maps (43) and simulated coherence maps for a simple displaced oscillator model (SFig. 7) we can assign this subset of BRC peaks to a purely vibrational origin. In contrast, the peaks labelled 1-4 in Figure 3 have no assignment within the simple displaced oscillator (SFig. 7)(7, 34, 55), electronic dimer(34) or vibronic dimer models that neglect the doubly-excited excitonic state (SFig. 8)(20, 27, 35). Peaks labeled 1 and 2 arise at an excitation energy corresponding to the lower exciton of the special pair (P-), while peaks 3 and 4 coincide with the excitation energy of the upper exciton P_+ (50). A notable departure from purely vibrational coherence is the lack of diagonal peaks associated with either P_- or P_+ . To understand the origin of peaks 1-4 we constructed a reduced vibronic model of the BRC.

Reduced Vibronic Model of the BRC

 $|g_{D}\rangle$

 $\omega_{\scriptscriptstyle B}$

Special Pair Excitons B BChla with vibrational mode $\omega_{B} \approx \omega_{P+} + \omega_{vib}$ $|g_{P}\rangle|e_{B}^{0}\rangle$ $|g_{P}\rangle|e_{B}^{0}\rangle$

 $|e_{p+}\rangle|g_{p}^{0}\rangle$

 $|g_{_{\mathrm{P}}}\rangle|g_{_{\mathrm{B}}}^{0}\rangle$

Figure 4 Reduced excitonic model of the BRC. (A) The site basis representation of the reduced Frenkel exciton model where the strongly coupled special pair molecules are represented by their delocalized excitonic states (|ep+), |ep-)) formed by electronic coupling between the special pair molecules, $J_{PP} = 325 \text{ cm}^{-1}$ (STab. 2). The nearest-neighbor accessory BChl ($|e_B\rangle$) additionally has one excited vibrational state on the ground ($|g_B|$) and excited ($|e_B|$) electronic states. The inhomogeneously broadened excited electronic state of B (|e_B⁰)) is represented with a Gaussian distribution of 100 cm⁻¹ width (blue gradient). (B) The collective state basis represents the same states as in part (A) demonstrating the near resonance of two key transitions: $|g_P\rangle|e_B^0\rangle$ and $|e_{P+}\rangle|g_B^1\rangle$. (C) The eigenstate basis includes electronic coupling, $J_{PB} = 100 \text{ cm}^{-1}$ (STab. 2), between the P and B sites and results in mixing between the two near-resonant transitions $|g_P\rangle|e_B^0\rangle$ and $|e_{P+}\rangle|g_B^1\rangle$. The electronic mixing enhances the allowedness of state $|p'\rangle$, which involves simultaneous excitation of the special pair excited state and the ground state coherence of B ($|e_{P+}\rangle|g_B^1\rangle$). Eigenstate $|p'\rangle$ is the key state giving rise to signatures 3 & 4 and the corresponding lower exciton special pair state in signatures 1 & 2 (Fig. 3). Parts (B) and (C) focus on the P upper exciton for visual simplicity; a more complete eigenstate diagram is presented in Fig. 6.

To assign and qualitatively describe the characteristic spectral features 1-4 associated with the measured coherence maps (Fig. 3), we employ an effective electronic three state model representing the two special pair (SP) BChl molecules (P_A and P_B in Fig. 1A) and one accessory BChl molecule denoted as B_A. The model is reduced in the number of states with respect to the full Frenkel exciton model of the BRC to minimize the time needed to simulate 2D spectra, as both

 $+ c_{2} |\mathbf{e}_{P+}\rangle |\mathbf{g}_{R}^{1}\rangle$

 $|g'\rangle$

 $|g\rangle$

averaging over energetic disorder and exploration of a large parameter space are required. We begin with an assumption that the interesting spectral features of the ω_2 maps are a result of the vibronic interaction between electronic states and intramolecular vibrational modes of the BRC chromophores, and we put this assumption to a test in our simulations.

Our reduced vibronic model considers a single intramolecular vibrational mode (with the same frequency as experimentally observed modes) placed either on B_A or one of the SP pigments (Fig. 4A). Parameters of the model are inspired by the excitonic model of Jordanides et al.(47), from which we take the orientations of the transition dipole moments and the electronic coupling energies between the B and SP molecules (47). The energies of the upper and lower SP excitons are taken from Ref. (50) and for simplicity we assume that the SP is a homodimer. This allows us to fix the coupling strength between its molecules and their excitation energies by the spectral positions of the excitonic states. The parameters of our model are listed in STable 2. We stress that the main aim of our simulations is not to reproduce the absorption and/or 2D spectra of the studied species, but rather to investigate the origin of the specific features 1-4 of the coherence maps. As a result, our reduced model of the BRC can only be expected to reproduce positions of specific features of the experimental absorption and 2D spectra (positions of the SP main peak, and the position of the B peak), and it is expected to fail in reproducing amplitudes of the peaks (e.g. the B transition must have roughly half the absorption since we neglect the second B, and the H transition is missing entirely since we neglect both H pigments). Due to its weak coupling, the influence of the intramolecular vibrational mode in the absorption and 2D spectra is very small and the impact of the intramolecular vibrational modes is only revealed in the coherence maps. We study three different frequencies of the vibrational mode and two different locations of the vibrations on the BRC molecules, however, the model only includes a single intramolecular vibrational mode at a time. Correspondingly, subtle mutual influences of vibrational modes are absent from our model, and it is expected that detailed features of experimental spectra will not be reproduced quantitatively.

2D Electronic spectra are calculated by first listing all Liouville pathways corresponding to the third order non-linear response of the simulated model system. We collect both rephasing and non-rephasing Liouville pathways for the ground state bleach (GSB), stimulated emission (SE) and excited state absorption (ESA) contributions to the 2D spectrum. We ignore the so-called double coherence contributions, which arise only during pulse overlap. Instead of calculating the full 2D spectra, we pre-select only those pathways which oscillate in the waiting time t_2 with the given frequency ω_2 of the vibrational mode and thus calculate only the part of the 2D spectrum that contributes to a selected coherence map. By such a procedure, which is based on inspecting states from which the pathways are composed without evaluating their contribution to the 2D spectrum, we remove the non-oscillating part of the signal and also the part of the spectrum oscillating at other frequencies. In this way we avoid evaluating Liouville pathways which are not expected to contribute to the final coherence map. The ignored pathways correspond to a majority of the total ensemble of pathways. We represent the simulated signals as 2D coherence maps and compare the resulting peak distributions to experiment in Figure 5.

We find that our reduced model reproduces the characteristic BRC peaks 1-4 in the experimental spectra (Fig. 3) only when the vibrational mode resides on the B pigment (Fig. 4A) rather than on one of the special pair pigments (Supplementary Fig. 18). This is unexpected, as the positions of the peaks suggest that the first excitation of the system involves P₊ or P₋, and appears unrelated to the formation of the vibrational coherence on B. To characterize the influence of resonance

between the vibrational frequency and the energy gaps we performed a parameter scan over the $P_+ - B$ energy gap, ΔE , for the three vibrational frequencies $\omega = 570$ cm⁻¹, 740 cm⁻¹ and 900 cm⁻¹. The results are presented in the form of movies (see STable 1) with the energy gap as a running parameter. In all three cases, the experimentally-observed peak pattern is reproduced in quasi-resonance conditions, when the electronic energy gap is smaller than the vibrational frequency. Exact resonance between the vibrational frequency and the electronic energy gap produces a dramatically different pattern that is inconsistent with the experimental observations.

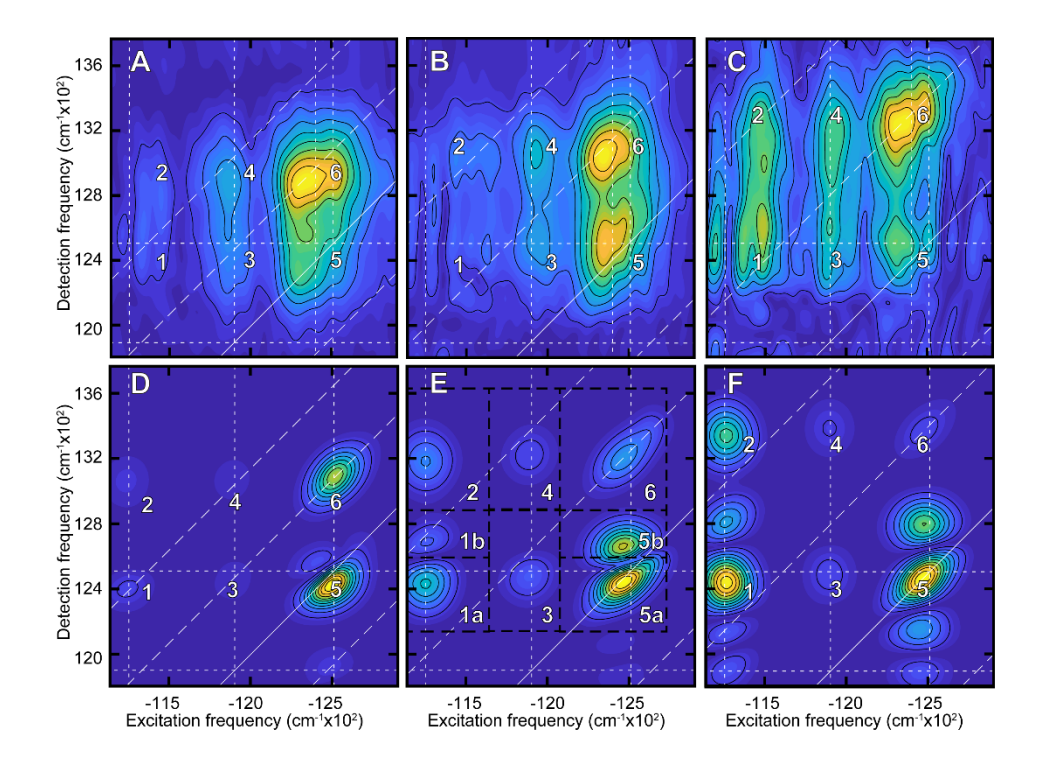


Figure 5 Comparison of experimental and simulated positive frequency coherence maps. Experimental (A-C) and simulated (D-F) complex rephasing coherence maps for $\omega_2 = +570$, +740, and +900 cm⁻¹ featuring the prominent signatures (labeled 1-6) of vibronic coherence between special pair and accessory BChl sites. Prominent pathways found in regions 1-6 detailed in Fig. 6.

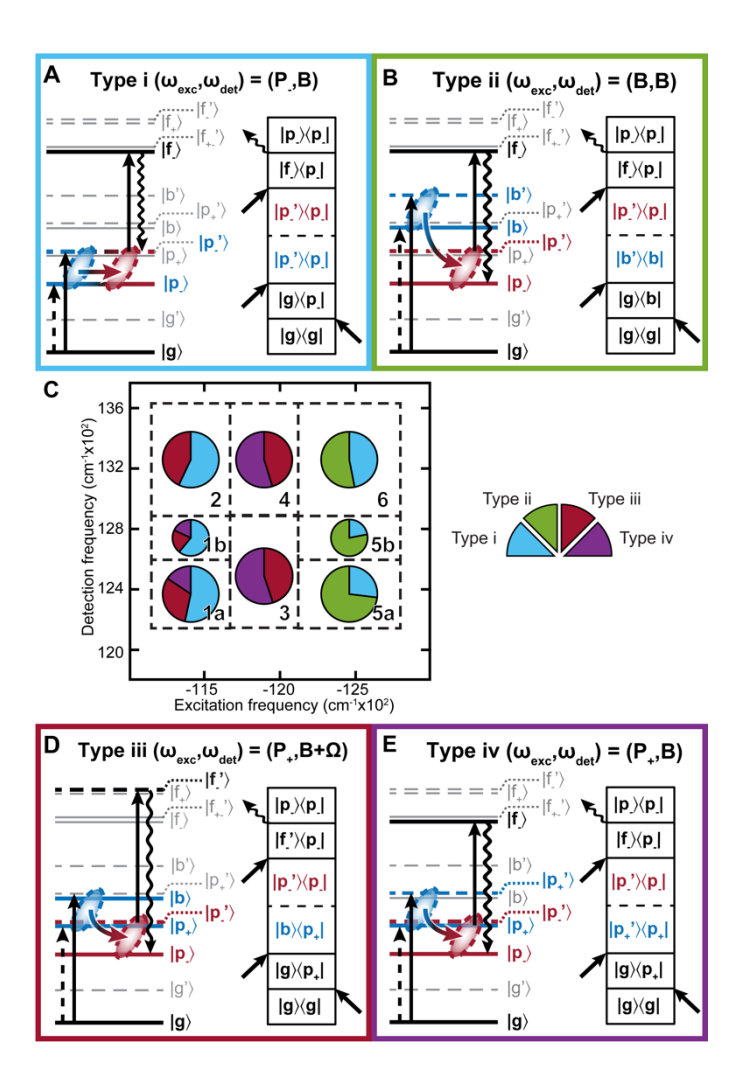


Figure 6 Prominent coherence pathways contributing to signals in regions 1-6. (A, B, D, E) Example dominant light-matter interaction pathways identified from simulations and represented both as light-matter Jablonski Diagrams (left) and Double-Sided Feynman Diagrams (right). (C) Cartoon coherence map showing the contribution of the four pathway types to each

spectral region 1-6.

Discussion

Features 1-4 in the coherence maps are clearly of a mixed, i.e. vibronic origin: they appear at ω_2 frequencies that match the vibrational frequency, and are absent in simulations where coupling between the SP and B_A is set to zero. From a detailed analysis of the Liouville pathways associated with each peak and the composition of the system eigenstates, we can conclude that the mixing between the electronic and vibrational states in the quasi-resonant case is rather weak. In quasiresonance, vibrational states can borrow oscillator strength from the electronic transitions by forming mixed vibrational-electronic (vibronic) eigenstates. It was previously found that the resonance condition for enhancement of vibrational coherence in 2DES is rather broad(27) and does not require an exact resonance between electronic and vibrational energy gaps. Under the quasi-resonance conditions, the observed oscillatory frequency is almost identical to the vibrational frequency of the original intramolecular mode and the eigenstates of the BRC largely keep their original electronic character such that the new energy gaps between eigenstates are not significantly changed by the level repulsion. However, some previously forbidden states, notably those containing vibrational excitation in the electronic ground state, acquire non-zero, albeit small, transition dipole moment (Fig. 4C). Crucially, the condition of quasi-resonance allows vibrational modes with a broad range of frequencies to have enhanced spectroscopic signatures. As a result, different coherence frequencies can produce similar patterns of coherence amplitude distribution in 2DES, consistent with our observations in Figure 3. The hallmark of the quasiresonant case is the "stable" ω_2 frequency of the features, which always corresponds to the vibrational frequency. In the resonant case, on the other hand, the frequency of the vibronic features can be shifted appreciably due to strong vibronic mixing. Additionally, the condition of resonance is not simultaneously possible with all three vibrational modes observed in the experiment.

Based on the simulations, we are able to assign a set of Liouville pathways to each peak labeled 1-6 in the experimental coherence maps (Figs 3 & 5). An extensive list of the associated Liouville pathways can be found in the Supplementary Materials. We highlight the four most prominent types of coherence signatures, most of which include coherence transfer (Fig. 6). While the coherences involved in these pathways are vibronic in nature, it is instructive to consider the leading excitonic or vibrational character in each case. These are: Type i): decaying vibrational coherence residing in the ground or excited state of the B molecule. Type ii): vibrational coherence shift from the excited state of B to its ground state accompanied by electronic energy transfer from the B molecule to the P- or P+ states. This process was previously identified by Paleček et al(30) and named Energy Transfer-Induced Coherence Shift (ETICS). Type iii): electronic to vibrational coherence transfer, in which an initial electronic coherence, such as the one between purely excitonic states of the B molecule and the P- state of the SP is transferred into a coherence characterized by a population of an excitonic state (e.g. P-) with a vibrational coherence in the ground state of the B molecule. These processes can also formally be regarded as a manifestation of ETICS. Type iv): ground-state vibrational coherence on B which acts as a spectator of the excited electronic dynamics occurring elsewhere in the system. The example Type iv pathway given in Figure 6E enables identification of the P+ state during energy relaxation from P+ to P-.

Our simulations (Fig. 5) confirm our assignment of peaks 1 and 2 to the Liouville pathways starting with the lower exciton state P₋ and peaks 3 and 4 to the upper exciton state P₊ (Fig. 3). The process of vibrational coherence decay denoted as Type i) is the leading contributor in terms of amplitude to peaks 1 and 2 of the calculated spectra (Fig. 6). The striking feature of this coherence is the fact

that although the process occurs nominally in the collective excited state of the BRC, it involves a vibrational mode excited in the electronic ground state of the B molecule. As is well-known, excitonic states involve a single molecular excitation (possibly delocalized over several molecules) while the remaining molecules of the aggregate remain unexcited. Due to resonance interaction between the molecules, some allowed excitonic states contain vibrational excitations on the electronic ground state of the participating molecules (see Fig. 4 and the SI for detailed information on the composition of vibronic eigenstates of the model BRC). To excite from the electronic (and vibrational) ground-state of the aggregate to what is effectively a ground state vibration, the present mechanism requires only a single interaction with the laser pulse. This makes the mechanism of vibronic enhancement at work here different from the one discussed by Tiwari et al.(20), where the observed oscillations are part of the ground-state bleach (GBS) signal wherein the vibrational coherence in the electronic ground state is excited after two interactions of the field with the system. Type i) coherence is more closely related to the excited state vibronic coherence described by Christensson et al.(27), with the distinction that the oscillating signal measured in the present work corresponds to excited state absorption rather than stimulated emission.

Peaks 3 and 4 (Fig. 3) are dominated by Liouville pathways involving energy transfer from state P+ to P- in a process of Type iv) (Fig. 6E). Here we first excite the state P+ and the vibrational coherence on the B molecule. During t2, population of P+ transfers to P- while the vibrational coherence in the ground state of the B molecule remains largely unaffected. However, its presence allows us to observe the energy relaxation process in the coherence map. Another dominant pathway contributing to peaks 3 and 4 is a type of ETICS process (Type iii)), an example of which is given in Figure 6D. A detailed account of the Liouville pathways identified in our simulations as leading contributions to signals 1-6 can be found in the SI.

We note the utility of Type iv) coherence in clearly revealing elusive states such as P₊. The P₊ state is weakly present in the real absorptive 2DES data (SFig. 2A) and was assigned to an energy of 11,900 cm⁻¹ after extensive kinetic analysis (50). In contrast, coherence analysis renders this state easy to detect. The assignment of P+ is notable given the difficulty of determining the location of P₊ in previous studies of BRCs. Experimental studies of R. sphaeroides locate P₊ between 12,225 $-12,642 \text{ cm}^{-1} (818 - 791 \text{ nm})(49, 56, 57)$ at 1.5-10 K and at 12,121 cm⁻¹ (825 nm) at room temperature(58), while a theoretical model predicts P₊ at 12,346 cm⁻¹ (810 nm) and 12,285 cm⁻¹ (814 nm) at 77 K and room temperature, respectively(47). The site energies and couplings of the special pair molecules also depend on experimental factors including temperature and solvent composition(4). The discrepancies between our assignment of 11,900 cm⁻¹ (840 nm) to P₊ in the R. capsulatus BRC and BRCs in other works may also be a result of differences between bacterial species studied. The ability to reveal signatures of dark states through coherence map analysis has been reported in 2DES (59) and 2D infrared spectroscopy studies(42). Vibrational coherence transfer has been previously reported in 2D IR experiments(41), 2DES studies of silver nanoclusters (40) and transient absorption experiments probing passage through conical intersections(39).

Vibronic coherence transfer identified in this work must be distinguished from electronic coherence transfer processes. While coherence transfer between excitonic states can be identified in photosynthetic systems with strong coupling to environment and substantially different reorganization energies on the involved molecular transitions (60, 61) and it has been proposed that coherence transfer contributions to 2DES signals can be significant in strongly-coupled systems (62), most theories of photosynthetic energy transfer have focused on population transfer,

ignoring coherence transfer processes and invoking the "secular approximation" (63). In the secular approximation the evolution of the populations and coherences are independent of each other, and coherence transfer processes are neglected: Liouville pathways involving excited or ground state coherence during the time interval t_2 can only decay, and cannot drive other coherences or populations, nor can they be fed from other coherences or populations. Electronic effects beyond the secular approximation are manifested spectroscopically, e.g., by temperature dependent absorption band shifts (60, 61). At a given temperature, however, these absorption band shifts can be understood as an effective localization of the system's excitonic states due to strong interaction with environment (i.e. as an effective reduction of coupling between involved molecular states). The electronic part of the system can thus be represented by an effective Hamiltonian accounting for energy and coupling renormalization. To this Hamiltonian a theory of electronic energy transfer in the secular approximation is applied. The vibronic states assigned in this work then represent superpositions of localized vibrational states and the states of the effective electronic Hamiltonian.

The spectroscopic signatures we observe in the BRC suggest the possible importance of electronic-vibrational resonances and coherence transfer processes involving vibrations on B. These vibrations may play a functional role in assisting the transfer of electronic excitation energy. Such a role for electronic-vibrational resonances has been proposed in other photosynthetic systems(19)·(20), as has their possible importance for downhill energy transfer from H to B in the BRC(30). Recent 2DES studies of BRCs have reported that particular low-frequency quasi-resonances (<200 cm⁻¹) between exciton and charge-transfer (CT) states are correlated with high charge separation efficiency(29, 32). However, the functional relevance of these quasi-resonances for charge separation remains a topic of debate (14, 26).

In conclusion, we report previously hidden excitonic and vibronic structure in the BRC, revealed through analysis of coherent 2DES signals. We confirm the assignment of the elusive special pair upper exciton state and find numerous quasi-electronic-vibrational resonances in the BRC. Through a comparison of the monomer BChl and BRC 2DES coherence maps along with simulations of a reduced BRC model we identify vibronic coherence transfer processes involving the special pair and B pigments, in which vibrations on B play a prominent role. The possible functional importance of such processes, as well as quasi-electronic-vibrational resonances to photosynthetic energy transfer and charge separation, merit further theoretical and experimental examination.

Materials and Methods

2DES Measurements

All experimental data presented here was collected using a hybrid pump-probe, background free 2DES setup which utilizes an acousto-optic programmable dispersive filter (AOPDF) pulse shaper (Dazzler, Fastlite) to simultaneously collect rephasing, nonrephasing, and transient grating signal(64). Interpulse delay between the first and second pump pulses were scanned $0 < t_1 < 390$ fs in 10 fs steps; waiting time between second pump and the probe, t_2 , was scanned in 10 fs steps from $-50 < t_2 < 3500$ fs. Data was truncated at $80 < t_2 < 3500$ fs prior to coherence analysis to eliminate contributions by coherent transients, resulting in a coherence frequency resolution of 9.8 cm⁻¹ and maximum resolvable coherence frequency of 1668 cm⁻¹. Light pulses were generated using a home-built optical parametric amplifier seeded by a 500 Hz, 40 fs, Tai:Sapph regen (SpitFire, Spectra Physics) centered at 800 nm. Both experiments used pumps, probe and local

oscillator from the same degenerate OPA (DOPA)(65) (spectra shown in SFig. 2). The pump used in the BRC (BChl) experiment was compressed to 14.5 (14.3) fs with an AOPDF and the probe to 10.3 (10) fs using chirped mirrors and a SLM pulse shaper (femtoJock, Biophotonics).

All experiments shown here were conducted at 77 K in a LN_2 cryostat (Microstat, Oxford Instruments) with a 380 μ m path length cell. Samples were prepared to have an average $OD \approx 0.3$, though the BRCs were prepared with higher peak OD in order to better resolve the lower dipole-strength special pair. BChl samples were prepared from powder purchased from Sigma Aldrich and were dissolved in isopropanol, which was degassed using N_2 gas before sample preparation. The sample was handled and loaded under N_2 atmosphere in a glove box.

Sample Preparation

W(M250)V BRC mutants were isolated and kept in pH 7.8 10 mM Tris with 0.1% Deriphat buffer. Prior to concentration, BRC samples were treated with 40 mM terbutryn in order to remove or inactivate quinones and 400 mM sodium ascorbate to reduce the special pair between laser shots. Following concentration, BRCs in buffer were mixed with glycerol (1:1 v/v) to ensure good quality glass when frozen.

References

- 1. R. E. Blankenship, *Molecular Mechanisms of Photosynthesis* (Blackwell Science Ltd, Oxford, UK, 2008).
- 2. W. W. Parson, A. Warshel, in *The Purple Phototrophic Bacteria*, C. N. Hunter, F. Daldal, M. C. Thurnauer, J. T. Beatty, Eds. (Springer Netherlands, Dordrecht, 2009; http://link.springer.com/10.1007/978-1-4020-8815-5), vol. 28 of *Advances in Photosynthesis and Respiration*, pp. 355–377.
- 3. C. A. Wraight, R. K. Clayton, The absolute quantum efficiency of bacteriochlorophyll photooxidation in reaction centres of Rhodopseudomonas spheroides. *BBA Bioenerg.* **333**, 246–260 (1974).
- 4. C. Kirmaier, D. Holten, W. W. Parson, Picosecond-photodichroism studies of the transient states in Rhodopseudomonas sphaeroides reaction centers at 5 K. Effects of electron transfer on the six bacteriochlorin pigments. *Biochim. Biophys. Acta Bioenerg.* **810**, 49–61 (1985).
- 5. L. M. Yoder, A. G. Cole, R. J. Sension, Structure and function in the isolated reaction center complex of Photosystem II: energy and charge transfer dynamics and mechanism. *Photosynth. Res.* **72**, 147–58 (2002).
- 6. T. Brixner, J. Stenger, H. M. Vaswani, M. Cho, R. E. Blankenship, G. R. Fleming, Two-dimensional spectroscopy of electronic couplings in photosynthesis. *Nature*. **434**, 625–628 (2005).
- 7. D. B. Turner, R. Dinshaw, K.-K. Lee, M. S. Belsley, K. E. Wilk, P. M. G. Curmi, G. D. Scholes, Quantitative investigations of quantum coherence for a light-harvesting protein at conditions simulating photosynthesis. *Phys. Chem. Chem. Phys.* **14**, 4857–74 (2012).
- 8. G. D. Scholes, G. R. Fleming, A. Olaya-Castro, R. Van Grondelle, Lessons from nature about solar light harvesting. *Nat. Chem.* **3**, 763–74 (2011).

- 9. K. L. M. Lewis, J. P. Ogilvie, Probing Photosynthetic Energy and Charge Transfer with Two-Dimensional Electronic Spectroscopy. *J. Phys. Chem. Lett.* **3**, 503–510 (2012).
- 10. G. S. Engel, T. R. Calhoun, E. L. Read, T.-K. Ahn, T. Mančal, Y.-C. Cheng, R. E. Blankenship, G. R. Fleming, Evidence for wavelike energy transfer through quantum coherence in photosynthetic systems. *Nature*. **446**, 782–786 (2007).
- 11. G. Panitchayangkoon, D. Hayes, K. A. Fransted, J. R. Caram, E. Harel, J. Wen, R. E. Blankenship, G. S. Engel, Long-lived quantum coherence in photosynthetic complexes at physiological temperature. *Proc. Natl. Acad. Sci.* **107**, 12766–12770 (2010).
- 12. M. H. Vos, J. C. Lambry, S. J. Robles, D. C. Youvan, J. Breton, J. L. Martin, Direct observation of vibrational coherence in bacterial reaction centers using femtosecond absorption spectroscopy. *Proc. Natl. Acad. Sci.* 88, 8885–9 (1991).
- 13. M. H. Vos, J. L. Martin, Femtosecond processes in proteins. *Biochim. Biophys. Acta-Bioenerg.* **1411**, 1–20 (1999).
- 14. E. Romero, V. I. Novoderezhkin, R. Van Grondelle, Quantum design of photosynthesis for bio-inspired solar-energy conversion. *Nature.* **543**, 355–365 (2017).
- 15. A. Ishizaki, G. R. Fleming, On the adequacy of the Redfield equation and related approaches to the study of quantum dynamics in electronic energy transfer. *J. Chem. Phys.* **130** (2009), doi:10.1063/1.3155214.
- 16. A. Ishizaki, G. R. Fleming, Unified treatment of quantum coherent and incoherent hopping dynamics in electronic energy transfer: Reduced hierarchy equation approach. *J. Chem. Phys.* **130** (2009), doi:10.1063/1.3155372.
- 17. A. W. Chin, Á. Rivas, S. F. Huelga, M. B. Plenio, Exact mapping between system-reservoir quantum models and semi-infinite discrete chains using orthogonal polynomials. *J. Math. Phys.* **51** (2010), doi:10.1063/1.3490188.
- 18. P. Huo, D. F. Coker, Iterative linearized density matrix propagation for modeling coherent excitation energy transfer in photosynthetic light harvesting. *J. Chem. Phys.* **133** (2010), doi:10.1063/1.3498901.
- 19. J. M. Womick, A. M. Moran, Vibronic Enhancement of Exciton Sizes and Energy Transport in Photosynthetic Complexes. *J. Phys. Chem. B.* **115**, 1347–1356 (2011).
- 20. V. Tiwari, W. K. Peters, D. M. Jonas, Electronic resonance with anticorrelated pigment vibrations drives photosynthetic energy transfer outside the adiabatic framework. *Proc. Natl. Acad. Sci.* **110**, 1203–8 (2013).
- 21. A. Kolli, E. J. O'Reilly, G. D. Scholes, A. Olaya-Castro, The fundamental role of quantized vibrations in coherent light harvesting by cryptophyte algae. *J. Chem. Phys.* **137**, 174109 (2012).
- 22. S. F. Huelga, M. B. Plenio, Vibrations, quanta and biology. *Contemp. Phys.* **54**, 181–207 (2013).
- 23. N. Renaud, D. Powell, M. Zarea, B. Movaghar, M. R. Wasielewski, M. A. Ratner, Quantum interferences and electron transfer in photosystem I. *J. Phys. Chem. A.* **117**, 5899–908 (2013).

- 24. F. D. Fuller, J. Pan, A. Gelzinis, V. Butkus, S. S. Senlik, D. E. Wilcox, C. F. Yocum, L. Valkunas, D. Abramavicius, J. P. Ogilvie, Vibronic coherence in oxygenic photosynthesis. *Nat. Chem.* **6**, 706–711 (2014).
- 25. E. Romero, R. Augulis, V. I. Novoderezhkin, M. Ferretti, J. Thieme, D. Zigmantas, R. Van Grondelle, Quantum coherence in photosynthesis for efficient solar-energy conversion. *Nat. Phys.* **10**, 676–682 (2014).
- 26. Y. Fujihashi, M. Higashi, A. Ishizaki, Intramolecular Vibrations Complement the Robustness of Primary Charge Separation in a Dimer Model of the Photosystem II Reaction Center. *J. Phys. Chem. Lett.*, 4921–4929 (2018).
- 27. N. Christensson, H. F. Kauffmann, T. Pullerits, T. Mančal, Origin of long-lived coherences in light-harvesting complexes. *J. Phys. Chem. B.* **116**, 7449–7454 (2012).
- J. Cao, R. J. Cogdell, D. F. Coker, H.-G. Duan, J. Hauer, U. Kleinekathöfer, T. L. C. Jansen, T. Mančal, R. J. D. Miller, J. P. Ogilvie, V. I. Prokhorenko, T. Renger, H.-S. Tan, R. Tempelaar, M. Thorwart, E. Thyrhaug, S. Westenhoff, D. Zigmantas, Quantum biology revisited. *Sci. Adv.* 6, eaaz4888 (2020).
- 29. S. Westenhoff, D. Paleček, P. Edlund, P. Smith, D. Zigmantas, Coherent Picosecond Exciton Dynamics in a Photosynthetic Reaction Center. *J. Am. Chem. Soc.* **134**, 16484–16487 (2012).
- 30. D. Paleček, P. Edlund, S. Westenhoff, D. Zigmantas, Quantum coherence as a witness of vibronically hot energy transfer in bacterial reaction center. *Sci. Adv.* **3**, 1–18 (2017).
- 31. M. L. Flanagan, P. D. Long, P. D. Dahlberg, B. S. Rolczynski, S. C. Massey, G. S. Engel, Mutations to R. sphaeroides Reaction Center Perturb Energy Levels and Vibronic Coupling but Not Observed Energy Transfer Rates. *J. Phys. Chem. A.* **120**, 1479–1487 (2016).
- 32. I. S. Ryu, H. Dong, G. R. Fleming, Role of electronic-vibrational mixing in enhancing vibrational coherences in the ground electronic states of photosynthetic bacterial reaction center. *J. Phys. Chem. B.* **118**, 1381–1388 (2014).
- 33. A. Chenu, N. Christensson, H. F. Kauffmann, T. Mančal, Enhancement of Vibronic and Ground-State Vibrational Coherences in 2D Spectra of Photosynthetic Complexes. *Sci. Rep.* **3**, 2029 (2013).
- 34. V. Butkus, D. Zigmantas, D. Abramavicius, L. Valkunas, Distinctive character of electronic and vibrational coherences in disordered molecular aggregates. *Chem. Phys. Lett.* **587**, 93–98 (2013).
- 35. V. Butkus, L. Valkunas, D. Abramavicius, Vibronic phenomena and exciton—vibrational interference in two-dimensional spectra of molecular aggregates. *J. Chem. Phys.* **140**, 034306 (2014).
- 36. A. Halpin, P. J. M. Johnson, R. Tempelaar, R. S. Murphy, J. Knoester, T. L. C. Jansen, R. J. D. Miller, Two-dimensional spectroscopy of a molecular dimer unveils the effects of vibronic coupling on exciton coherences. *Nat. Chem.* **99**, 0–5 (2014).

- 37. D. A. Farrow, W. Qian, E. R. Smith, A. A. Ferro, D. M. Jonas, Polarized pump-probe measurements of electronic motion via a conical intersection. *J. Chem. Phys.* **128**, 144510 (2008).
- 38. J. Brazard, L. A. Bizimana, T. Gellen, W. P. Carbery, D. B. Turner, Experimental Detection of Branching at a Conical Intersection in a Highly Fluorescent Molecule. *J. Phys. Chem. Lett.* **7**, 14–19 (2016).
- 39. A. J. Musser, M. Liebel, C. Schnedermann, T. Wende, T. B. Kehoe, A. Rao, P. Kukura, Evidence for conical intersection dynamics mediating ultrafast singlet exciton fission. *Nat. Phys.* **11**, 352–357 (2015).
- 40. E. Thyrhaug, S. A. Bogh, M. R. Carro-Temboury, C. S. Madsen, T. Vosch, D. Zigmantas, Ultrafast coherence transfer in DNA-templated silver nanoclusters. *Nat. Commun.* **8**, 15577 (2017).
- 41. M. J. Nee, C. R. Baiz, J. M. Anna, R. McCanne, K. J. Kubarych, Multilevel vibrational coherence transfer and wavepacket dynamics probed with multidimensional IR spectroscopy. *J. Chem. Phys.* **129**, 084503 (2008).
- 42. P. A. Eckert, K. J. Kubarych, Vibrational coherence transfer illuminates dark modes in models of the FeFe hydrogenase active site. *J. Chem. Phys.* **151**, 054307 (2019).
- 43. V. R. Policht, A. Niedringhaus, J. P. Ogilvie, Characterization of Vibrational Coherence in Monomeric Bacteriochlorophyll a by Two-Dimensional Electronic Spectroscopy. *J. Phys. Chem. Lett.* **9**, 6631–6637 (2018).
- 44. D. M. Jonas, Two-Dimensional Femtosecond Spectroscopy. *Annu. Rev. Phys. Chem.* **54**, 425–463 (2003).
- 45. K. M. Faries, N. P. Dylla, D. K. Hanson, D. Holten, P. D. Laible, C. Kirmaier, Manipulating the Energetics and Rates of Electron Transfer in Rhodobacter capsulatus Reaction Centers with Asymmetric Pigment Content. *J. Phys. Chem. B.* **121**, 6989–7004 (2017).
- 46. M. H. B. Stowell, T. M. McPhillips, D. C. Rees, S. M. Soltis, E. Abresch, G. Feher, Light-Induced Structural Changes in Photosynthetic Reaction Center: Implications for Mechanism of Electron-Proton Transfer. *Science* (80-.). 276, 812–816 (1997).
- 47. X. J. Jordanides, G. D. Scholes, G. R. Fleming, The Mechanism of Energy Transfer in the Bacterial Photosynthetic Reaction Center. *J. Phys. Chem. B.* **105**, 1652–1669 (2001).
- 48. O. Rancova, R. Jankowiak, A. Kell, M. Jassas, D. Abramavicius, Band Structure of the Rhodobacter sphaeroides Photosynthetic Reaction Center from Low-Temperature Absorption and Hole-Burned Spectra. *J. Phys. Chem. B.* **120**, 5601–5616 (2016).
- 49. J. Breton, A. Vermeglio, *The Photosynthetic Bacterial Reaction Center* (Springer US, Boston, MA, 1988; http://ebooks.cambridge.org/ref/id/CBO9781107415324A009), vol. 149.
- 50. A. Niedringhaus, V. R. Policht, R. Sechrist, A. Konar, P. D. Laible, D. F. Bocian, D. Holten, C. Kirmaier, J. P. Ogilvie, Primary processes in the bacterial reaction center probed by two-dimensional electronic spectroscopy. *Proc. Natl. Acad. Sci.* 115, 3563–3568 (2018).

- 51. K. Czarnecki, J. R. Diers, V. Chynwat, J. P. Erickson, H. a. Frank, D. F. Bocian, Characterization of the Strongly Coupled, Low-Frequency Vibrational Modes of the Special Pair of Photosynthetic Reaction Centers via Isotopic Labeling of the Cofactors. *J. Am. Chem. Soc.* **119**, 415–426 (1997).
- 52. J. R. Diers, D. F. Bocian, Qy-Excitation Resonance Raman Spectra of Bacteriochlorophyll Observed under Fluorescence-Free Conditions. Implications for Cofactor Structure in Photosynthetic Proteins. *J. Am. Chem. Soc.* **117**, 6629–6630 (1995).
- 53. M. Lutz, J. Kleo, F. Reiss-Husson, Resonance raman scattering of bacteriochlorophyll, bacteriopheophytin and spheroidene in reaction centers of Rhodopseudomonas spheroides. *Biochem. Biophys. Res. Commun.* **69**, 711–717 (1976).
- 54. V. Palaniappan, C. C. Schenck, D. F. Bocian, Low-Frequency Near-Infrared-Excitation Resonance Raman Spectra of (M)H202L Mutant Reaction Centers from Rhodobacter sphaeroides. Implications for the Structural, Vibronic, and Electronic Properties of the Bacteriochlorin Cofactors. *J. Phys. Chem.* **99**, 17049–17058 (1995).
- 55. D. Egorova, Detection of electronic and vibrational coherences in molecular systems by 2D electronic photon echo spectroscopy. *Chem. Phys.* **347**, 166–176 (2008).
- 56. S. R. Meech, A. J. Hoff, D. A. Wiersma, Role of charge-transfer states in bacterial photosynthesis. *Proc. Natl. Acad. Sci.* **83**, 9464–9468 (1986).
- 57. G. Hartwich, H. Scheer, V. Aust, A. Angerhofer, Absorption and ADMR studies on bacterial photosynthetic reaction centres with modified pigments. *Biochim. Biophys. Acta Bioenerg.* **1230**, 97–113 (1995).
- 58. D. C. Arnett, C. C. Moser, P. L. Dutton, N. F. Scherer, The First Events in Photosynthesis: Electronic Coupling and Energy Transfer Dynamics in the Photosynthetic Reaction Center from Rhodobacter sphaeroides. *J. Phys. Chem. B.* **103**, 2014–2032 (1999).
- 59. A. A. Bakulin, S. E. Morgan, T. B. Kehoe, M. W. B. Wilson, A. W. Chin, D. Zigmantas, D. Egorova, A. Rao, Real-time observation of multiexcitonic states in ultrafast singlet fission using coherent 2D electronic spectroscopy. *Nat. Chem.* **8**, 16–23 (2016).
- 60. T. Renger, Theory of Optical Spectra Involving Charge Transfer States: Dynamic Localization Predicts a Temperature Dependent Optical Band Shift. *Phys. Rev. Lett.* **93**, 188101 (2004).
- 61. T. Mančal, L. Valkunas, G. R. Fleming, Theory of exciton—charge transfer state coupled systems. *Chem. Phys. Lett.* **432**, 301–305 (2006).
- 62. K. Hyeon-Deuk, Y. Tanimura, M. Cho, Ultrafast exciton-exciton coherent transfer in molecular aggregates and its application to light-harvesting systems. *J. Chem. Phys.* **127**, 075101 (2007).
- 63. V. May, O. Kuhn, *Charge and Energy Transfer Dynamics in Molecular Systems* (Wiley, 2011).
- 64. F. D. Fuller, D. E. Wilcox, J. P. Ogilvie, Pulse shaping based two-dimensional electronic spectroscopy in a background free geometry. *Opt. Express.* **22**, 1018 (2014).

- 65. A. M. Siddiqui, G. Cirmi, D. Brida, F. X. Kärtner, G. Cerullo, Generation of <7 fs pulses at 800 nm from a blue-pumped optical parametric amplifier at degeneracy. *Opt. Lett.* **34**, 3592 (2009).
- 66. J. R. Diers, Y. Zhu, R. E. Blankenship, D. F. Bocian, Qy-excitation resonance Raman spectra of chlorophyll a and bacteriochlorophyll c/d aggregates. Effects of peripheral substituents on the low-frequency vibrational characteristics. *J. Phys. Chem.* **100**, 8573–9 (1996).
- 67. J. Seibt, T. Pullerits, Beating signals in 2D spectroscopy: Electronic or nuclear coherences? application to a quantum dot model system. *J. Phys. Chem. C.* **117**, 18728–18737 (2013).
- 68. Y. Song, C. Hellmann, N. Stingelin, G. D. Scholes, The separation of vibrational coherence from ground- and excited-electronic states in P3HT film. *J. Chem. Phys.* **142**, 212410 (2015).
- 69. V. Butkus, D. Zigmantas, L. Valkunas, D. Abramavicius, Vibrational vs. electronic coherences in 2D spectrum of molecular systems. *Chem. Phys. Lett.* **545**, 40–43 (2012).
- 70. S. S. Senlik, V. R. Policht, J. P. Ogilvie, Two-Color Nonlinear Spectroscopy for the Rapid Acquisition of Coherent Dynamics. *J. Phys. Chem. Lett.* **6**, 2413–2420 (2015).
- 71. G. Lindblad, Completely positive maps and entropy inequalities. *Commun. Math. Phys.* **40**, 147–151 (1975).
- 72. B. Fain, *Irreversibilities in Quantum Mechanics* (Kluer Acadenic Publishers, Dorderecht, 2000).
- 73. S. Mukamel, *Principles of Nonlinear Spectroscopy* (Oxford University Press, Oxford, 1995).
- 74. T. Mančal, A decade with quantum coherence: How our past became classical and the future turned quantum. *Chem. Phys.* **532**, 110663 (2020).
- 75. J. Olšina, T. Kramer, C. Kreisbeck, T. Mančal, Exact stochastic unraveling of an optical coherence dynamics by cumulant expansion. *J. Chem. Phys.* **141**, 164109 (2014).
- 76. T. Mančal, J. Dostál, J. Pšenčík, D. Zigmantas, Transfer of vibrational coherence through incoherent energy transfer process in Förster limit. *Can. J. Chem.* **92**, 135–143 (2014).

Acknowledgments

Funding:

National Science Foundation grant PHY-0748470 (VRP, AN, JPO)

National Science Foundation grant PHY-1607570 (VRP, AN, JPO)

Office of Basic Energy Sciences, the US Department of Energy grant DE-SC0016384 (JPO)

U. S. Department of Energy, Office of Basic Energy Sciences grant DE-CD0002036 (CK, DH)

U. S. Department of Energy, Office of Basic Energy Sciences under Field Work Proposal DE-CD0002036 (PDL)

Charles University Research Center Program UNCE/SCI/010 (TM)

Czech Science Foundation (GAČR) grant 20-011595 (TM)

Author contributions:

Conceptualization: VRP, AN, JPO

Methodology: TM

Investigation: VRP, AN

Resources: PDL, CK, DH

Writing—original draft: VRP, JPO

Competing interests:

The authors declare no competing interests.

Data and materials availability:

All data are available in the main text or the supplementary materials.



advances.sciencemag.org/cgi/content/full/sciadv.[ms.no.]/DC1

Supplementary Materials for

Hidden Vibronic and Excitonic Structure and Vibronic Coherence Transfer in the Bacterial Reaction Center

Veronica Policht, Andrew Niedringhaus, Rhiannon Willow, Philip D. Laible, David F. Bocian, Dewey Holten, Christine Kirmaier, Tomáš Mančal, and Jennifer P. Ogilvie*

*Corresponding author. Email: jogilvie@umich.edu

This PDF file includes:

Supplementary Text Figs. S1 to S18 Tables S1 to S5 References (67 to 67)

Other Supplementary Materials for this manuscript include the following:

Movies S1 to S3

Science Advances Manuscript Template Page 22 of 70

Supplementary Text

Structure of the Bacterial Reaction Center

The structure of the Rb. sphaeroides RC in Figure 1 reveals the pseudo-twofold-symmetric structure of the RC (figure prepared using PyMOL with data from PDB entry 1AIJ(46)). The primary electron donor (P) is comprised of two bacteriochlorophyll a (BChl) molecules (PA and P_B) that are in van der Waals contact and form what is often termed the special pair (SP). P is flanked by two monomeric BChls (B_A and B_B) and two monomeric bacteriopheophytin a molecules (H_A and H_B). Due to the strong interactions between the two macrocycles of P, the electronic excited states of P are commonly described as being linear combinations of two locally-excited configurations (P_A* and P_B*) and two charge-transfer configurations (P_A+P_B- and P_A-P_B⁺). In our simple model which does not simulate charge separation, we neglect the charge transfer configurations, but find that weak coupling to a B pigment with ground and excited vibrational levels is necessary to reproduce our observed coherence maps. (See Supplementary Tables 2 and 4 for the reduced exciton model parameters and state compositions). Throughout our study, we refer to the eigenstates of the diagonalized Hamiltonian as the exciton states. Two of the excitons are found to be dominated by linear combinations of the excited P pigments. The lowest energy of these is often referred to simply as the "lower exciton state of P" and is denoted $P_{-} \sim (P_A^* - P_B^*)/\sqrt{2}$. Similarly, the higher energy state is often referred to simply as the "upper exciton state of P" and is denoted $P_{+}\sim (P_A^* + P_B^*)/\sqrt{2}$. The charge-separation events in the RC are initiated from P₋, either by direct excitation of P₋, by electronic relaxation from P₊, or by energy transfer from the exciton states involving electronic excitation of BA, BB, HA, or HB.

Experimental Details

Materials and Methods

All experimental data presented here was collected using a hybrid pump-probe, background-free 2DES setup which utilizes an acousto-optic programmable dispersive filters pulse shaper (Dazzler, Fastlite) to simultaneously collect rephasing, nonrephasing, and transient grating signals(64). For all experiments presented the coherence time between the two pump pulses, t_1 , was scanned from $0 < t_1 < 390$ fs in 10 fs steps; the waiting time between the pumps and probe, t_2 , was scanned from $-50 < t_2 < 3500$ fs in 10 fs steps. Both the pumps, probe, and local oscillator were generated from a single home-built Degenerate Optical Parametric Amplifier (DOPA)(65) seeded by a 500 Hz, 40 fs Ti:Sapph regenerative amplifier (SpitFire, Spectra Physics); the resulting DOPA light is centered at 800 nm with nearly 200 nm of bandwidth. The DOPA light was split by an 80/20 beam splitter into the pump and probe paths and were each partially compressed with chirped mirrors. The pump beam was compressed to 14.5 (14.3) fs with the Dazzler pulse shaper and the probe beam was compressed using a SLM pulse shaper (femtoJock, Biophotonics) to 10.3 (10) fs for the BRC (BChl) experiment. The pump and probe beams had 10.9 (7.3) and 14.1 (11.1) μ W of power for the BRC (BChla) experiments and spot sizes of 0.0278 (0.0299) and 0.0203 (0.0159) mm².

The *Rho. capsulatus* mutant W(M250)V BRC samples lack the A-branch quinone. Prior to concentration, the BRCs were treated with 40 mM terbutryn in ethanol to inactivate the B-branch quinone and 400 mM sodium ascorbate in buffer to reduce the special pair between laser shots. Concentrated RCs in 7.8 pH 10 mM Tris with 0.1% deriphat were mixed with glycerol to achieve a 1:1 (v:v) mixture for good optical quality glass upon freezing. The BRCs were prepared to achieve high enough S/N in the P band OD(860 nm) = 0.17 at room temperature; subsequently the B-band OD is OD(800 nm) = 0.36 at room temperature. Monomeric samples

were prepared in a nitrogen gas filled glove box by dissolving powdered BChl a purchased from Sigma Aldrich in isopropanol for OD(777 nm) = 0.4.

Additional Experimental Coherence Maps

Coherence Analysis

With the exception of SFigure 2 and SFigure 6, all of the data presented in this manuscript is of the real or complex rephasing signal. In order to resolve coherent dynamics, we scan the waiting time (t_2) with evenly-spaced 10 fs steps from -50 to 3500 fs. A 10 fs Δt_2 yields a maximum resolvable coherence frequency, ω_2 of 1,668 cm⁻¹. The data are truncated at t_2 = 80 fs in order to eliminate any contributions from coherent transient signals around t_2 = 0 fs, yielding a coherence frequency resolution of $\Delta \omega_2$ = 9.8 cm⁻¹. The kinetics contributions are fit using a global algorithm which simultaneously fits multiple exponential and complex oscillatory terms. The kinetic fit is subtracted from the data leaving only the oscillatory residual. The residual coherence signals for the BRC are less than 10% of the full signal containing the kinetic signals. The oscillatory residual is then Fourier transformed with respect to t_2 yielding a three-dimensional frequency solid. To quantify the dominant coherent modes present we take the Frobenius norm:

$$||S(\omega_2)|| = \sqrt{\sum_{i=1}^{\infty} \sum_{j=1}^{\infty} |S(\omega_{\text{exc},i}, \omega_2, \omega_{\text{det},j})|^2}$$

where i and j index over the excitation and detection frequency dimensions. The resulting Frobenius spectrum (Fig. 2A) shows the dominant coherent modes present. Positive and negative frequency maps (SFigure 4 & SFigure 5) were generated by performing the coherence analysis with the complex rephasing signal.

Additional Real Rephasing Coherence Maps

SFigure 3 presents the real rephasing signals of the two most prominent low frequency modes ($\omega_2 = 189 \& 336 \text{ cm}^{-1}$) for the BRC and BChl samples. The $\omega_2 = 189 \text{ cm}^{-1}$ map of for the BRC shows a node along the diagonal not present in the BChl experiment. In contrast, the $\omega_2 = 336 \text{ cm}^{-1}$ maps look similar for both maps. SFigure 3 additionally shows the coherence map for $\omega_2 = 656 \text{ cm}^{-1}$. The $\omega_2 = 656 \text{ cm}^{-1}$ is a weak mode in the BRC Frobenius spectrum (Fig. 2A) because it is a vibrational mode unique to the bacteriopheophytin a (BPheo) molecules(53) not present in resonance Raman of BChl(52, 66) and the coherence spectra of BRC are dominated by contributions from the B BChls. The $\omega_2 = 656 \text{ cm}^{-1}$ mode has been previously observed in oxidized BRCs and was assigned as a signature of vibronic coupling between the B and H molecules using a cross polarization scheme(29, 30). In our all-parallel polarization data, the $\omega_2 = 656 \text{ cm}^{-1}$ shows substantial signal amplitude in the B region of the spectrum. Because this mode does not belong to a vibrational mode of BChl but rather the H BPheo molecules, our data supports the previous assignments of vibronic coupling between the B and H molecules(29, 30).

Positive and Negative Frequency Maps of Complex Rephasing Signals

Each of the six coherence frequencies of the real rephasing signals presented in the main text (Fig. 3) and supplementary information (SFig. 3) are additionally presented with the complex rephasing signal (SFig. 4 & 5) where different signatures are separated between the positive and negative frequency. This type of complex coherence analysis was first proposed by Seibt and Pullerits(67) and implemented by Song, et al.(68). This method of coherence analysis has recently enabled greater certainty in assigning the origin of coherences in oxidized BRCs(30).

The complex rephasing 2D maps of monomeric BChl in SFigure 5 show excellent agreement with the simple displaced oscillator model of purely vibrational coherence in SFigure 7. Further discussion of the vibrational assignment of the coherences in this BChl sample are detailed in Policht, et.al.(43). Similar to the effects discussed in Palecek, et al.(30) we see that the signal nodes present along the diagonal of the real rephasing maps for both the BRC and BChl (Fig. 3 & SFig. 3) are not present in the individual positive and negative complex rephasing signal, indicating that signal nodes are due to destructive interference between $+\omega_2$ and $-\omega_2$ signals. In Palecek, et.al.(30) the destructive interference behavior was attributed to rapid energy transfer, though this explanation is not satisfactory for the monomeric BChl samples. Comparing the complex rephasing 2D maps of the BRC to the standard toy models of coherence (SFig. 7 & 8) we can determine that the signals 1-4 highlighted in Figure 3 of the main text do not arise from a simple displaced oscillator nor a vibronic model.

Nonrephasing Coherence Maps for M250V BRC

Coherence analysis of 2DES data typically focuses on coherence signatures in the rephasing signals. The coherence signatures in the nonrephasing signals provides analogous information as the rephasing signals though typically with a lower signal strength. For example, in the case of the model for purely vibrational coherence (SFig. 7), the nonrephasing coherence map would reproduce the characteristic "chair" pattern but reflected across the electronic transition energy, resulting in an upside-down chair with nonrephasing light-matter interaction pathways analogous to those numerated in SFigure 7. To demonstrate the ability of the reduced BRC model to reproduce the experimental results, we additionally present the real and complex nonrephasing coherence maps for the three mid-frequency modes presented in the main text (Fig. 3) in SFigure 6. A direct comparison to the nonrephasing signals from the theoretical simulations can be found in SFigure 18.

Toy Models for Coherence Modelling

Displaced Harmonic Oscillator

The displaced harmonic oscillator (SFig. 7) consists of two electronic states $|g\rangle$ and $|a\rangle$ separated by transition frequency A and displaced along nuclear coordinate q by some value d and allows for strong Franck-Condon overlap between different vibrational states of a vibration with frequency $|\Omega|$. Coherence signals oscillate at $|\Omega|$ and are arranged in a characteristic "chair" configuration with individual signals spaced apart by Ω . This model has been used extensively in simulations of molecular coherence measured using 2DES(7, 34, 55, 69) and has been used to assign the origin of coherences in chlorophyll a(70) and BChl(43).

Vibronically Coupled Displaced Oscillator

Another type of coherence often discussed in studies of coherence in photosynthetic systems is mixed electronic-vibrational, or vibronic, coherence. Vibronic coherence signals are often described by a pair of strongly coupled displaced harmonic oscillators with one active vibrational quantum per electronic state (SFig. 8). The vibronic model has been studied extensively(20, 27, 35) and has been invoked to explain the origin of coherences in several photosynthetic protein systems(20, 24, 25, 30). Coherence signals due to this model oscillate at several frequencies; that of the vibrational mode, $|\Omega|$; the excitonic difference frequency, $|\Delta E|$; and the sum and difference frequencies of the vibrational and exciton difference frequency, $|\Omega \pm \Delta E|$. In the case of degeneracy, $\Omega \approx \Delta E$, the number of distinct frequencies decreases from four to two ($\Omega \approx \Delta E$, $2*\Omega \approx 2*\Delta E$). In the case of near degeneracy, it is expected that the

coherence maps for $\Omega \approx \Delta E$ will feature two "chair" configurations aligned to the two singly excited electronic transitions (shown as shaded ovals marked "intramolecular vibrational coherence", where the diagonal elongation reflects inhomogeneous broadening of the A and B transitions). In the case of two uncoupled displaced oscillators these would be the only observable signals, however in this vibronic model there will also be cross terms which result from the shared ground state and which lie between the equally-spaced "chair" signals.

Theoretical Foundations of the Simulations

Theoretical Basis of Interpretation of 2DES

Nonlinear spectroscopic techniques, such as two-dimensional electronic spectroscopy (2DES), are intimately linked with their corresponding order of perturbation theory in the lightmatter interaction energy. This perturbation theory is most conveniently described using the density matrix (statistical operator) formalism. All the spectroscopic signal components in the third order 2DES can be expressed as sequences, also called Liouville pathways, of light-induced transitions between electronic eigenstates of the investigated system. For the photosynthetic molecular aggregates, such as the BRC we study here, electronic eigenstates are delocalized (to various degrees) over several molecules, depending on the strengths of the intermolecular interactions and the differences between the molecular energy gaps. We use the term exciton, excitonic state, or single exciton state equivalently for the energy eigenstates of the BRC. We denote the excited states, which individual molecules of the aggregate exhibit in absence of coupling to other molecules, as locally excited states, alluding to their absence of delocalization. The delocalized excitons correspond to quantum mechanical superpositions of the locally excited states.

In the experiment, the BRC is initially found in its electronic ground-state, and it is excited by a sequence of three laser pulses with two controllable delays t_1 and t_2 . The excitation pulses are intentionally kept at an appropriate intensity such that the observed signal depends at most cubically on the excitation field. From the total signal we disentangle a subset of the signal, which depends linearly on the electric field of each of the three incoming laser pulses, by the procedure of phase-cycling. Three pulses thus result in a third order signal. In the theoretical description of the measured signals, the bookkeeping of the perturbations (light-induced transitions) is done using the two indices of the density matrix describing the state of the molecular system. Each unique Liouville pathway is characterized by a unique sequence of density matrix indices (or more precisely pairs of indices), which we conveniently represent in the so-called double-sided Feynman diagrams (see Fig. 6 and SFig. 1). The diagram is composed of two vertical lines representing time progressing from the bottom up (SFig. 1). Each straight arrow attached to the sides of the Feynman diagram corresponds to an action of the laser field, and it is accompanied by a change of the system state. At each time (i.e. at each horizontal position), two states are denoted in the diagram representing the elements of the density matrix. The first two sections (from the bottom) of the Feynman diagrams (sections are separated by solid horizontal lines) correspond to delays t_1 and t_2 between the excitation pulses, the third section of the diagram corresponds to the time denoted as t_3 , at which the signal is detected. The origin of time, $t_3 = 0$, is set to coincide with the arrival time of the intensity maximum of the third laser pulse of the excitation. The signal is detected in the frequency domain, and the detection time is related by Fourier transform to the detection frequency denoted ω_3 .

Due to its perturbative nature, individual Liouville pathways combine information about the time evolution of three different elements of the system's density matrix. These elements in turn

carry information about light-induced processes in the studied system. The first section of the Feynman diagram corresponds to the evolution of coherence between the electronic ground state and a single-exciton state. This information translates into the peak lineshape in the ω_1 dimension of the 2D spectrum. The second section of the Feynman diagram corresponds to the time evolution of the studied system either in the electronic ground state or in the excited state (excited state evolution is depicted in SFig. 1B). If energy transfer occurs between the eigenstates of the system during time interval t_2 , the second section of the Feynman diagram is characterized by two sets of indices corresponding to the initial (immediately after the second pulse) and final (immediately before the third pulse) pairs of density matrix indices. The final section of the Feynman diagram displays the time evolution (in time t_3) of another coherence element of the density matrix, this time corresponding to the processes of stimulated emission (SE), ground state bleach (GSB) or excited state absorption (ESA). This translates into the ω_3 dimension of the 2D lineshape. The 2D spectrum represents the system's time evolutions in t_1 and t_3 as 2D lineshapes, while the evolution in the time t_2 is usually represented directly in the time domain. A sequence of 2D spectra in t_2 thus provides time-dependent information about the photo-induced state dynamics of the system. This state is fully described by the evolution of the state populations (diagonal elements of the density matrix) and the coherences between the states (off-diagonal elements of the density matrix). Interaction between the light and matter is of resonance character, and it addresses the effective eigenstates of the studied system. Populations and coherences of the system thus have to be understood as defined in the basis of effective system eigenstates, the so-called excitonic basis. In our simulations, we identify the effective system eigenstates with the eigenstates of our model Hamiltonian, which includes the electronic degrees of freedom and a selected vibrational mode. In the theory of photosynthetic aggregates, it is often found that the so-called secular approximation holds; namely that the evolutions of the populations and coherences, as well as those of different coherences, are independent of each other. In the secular approximation, Liouville pathways involving excited or ground state coherence during the time interval t_2 can only decay, and cannot drive other coherences or populations, nor can they be fed from other coherences or populations. The present study finds that when intramolecular vibrations interact with the electronic states of BChl molecules, the secular approximation no longer holds and the related nonsecular dynamics are responsible for most of the interesting spectral features we observe.

Conditions of Agreement between Experiment and Theory

The experimental ω_2 -maps of frequencies 570, 740 and 900 cm-1 (Fig. 3) share certain specific peak arrangements whose general features are subject to comparison to the theoretical spectra. We study the ω_2 -maps obtained by complex Fourier transform (FT) of a series of waiting time (t₂) dependent 2D spectra. In particular we examine the absolute value of the FT of the rephasing spectra at frequencies $+\omega_2$ and $-\omega_2$ (RPH+ and RPH- spectra, respectively) and non-rephasing spectra at frequencies $+\omega_2$ and $-\omega_2$ (NR+ and NR- spectra, respectively). These experimental maps exhibit characteristic patterns, which we compare to the patterns corresponding to our reduced model of BRC with a single vibrational mode assigned either to the B molecule or one of the SP molecules. We will consider the theoretical simulations to be in reasonable agreement with experiment if they can produce peaks of a pattern similar to the experiment in all the four types of ω_2 -maps. We will be able to assign the vibrations to the particular molecules (to SP or B) if the agreement of the theory with experiment appears exclusively in one assignment and not in the other.

Model Hamiltonian

We simulate 2D spectra and calculate ω_2 -maps from them using a reduced BRC model, which can be described by the following extended Frenkel exciton Hamiltonian

$$H = (E_g + H_{vib})|g\rangle\langle g| + \sum_k (E_k + \xi_k \hbar \omega dq)|k\rangle\langle k| + \sum_{kl} J_{kl} |k\rangle\langle l|. \tag{1}$$

Here, the Hamiltonian H_{vib} of the vibrational mode with frequency ω reads as

$$H_{vib} = \frac{\hbar\omega}{2} (p^2 + q^2). \tag{2}$$

The mode is coupled to a single molecule in the model, so that only one of all possible constants ξ_k is equal to 1, whereas all other ξ s are equal to zero. The strength of the coupling between the electronic energy gaps and the vibrational mode is characterized by the dimensionless parameter, the so-called Huang-Rhys factor

$$S = \frac{1}{2}d^2. \tag{3}$$

The states $|k\rangle$ represent electronic states of the RC. The Hamiltonian (Eq. (1)) is diagonalized to obtain vibronic eigenstates of the system, on which the calculation of the 2D spectra is based. See the SI section entitled **Detailed analysis of the 740 cm⁻¹ mode** for details of the eigenstates.

Energy Transfer and Dephasing

In order to simulate the spectroscopic response of the model system, we calculate time evolution of excited state and optical coherence blocks of the reduced electronic statistical operator (density matrix) $\rho(t)$ of the system. The blocks are composed of the matrix elements $\langle n|\rho(t)|g\rangle$ (optical coherence block, where $|g\rangle$ is the electronic ground state of the system and $|n\rangle$ are electronic excited states of the system) and $\langle n|\rho(t)|m\rangle$ (excited state block, where $|n\rangle$ and $|m\rangle$ are electronic excited states of the system). We propagate the reduced density matrix equation of motion in the form

$$\frac{\partial}{\partial t}\rho(t) = -\frac{i}{\hbar}[H_{el}, \rho(t)]_{-} + \mathcal{D}(t)\rho(t), \tag{4}$$

where H_{el} is the electronic Hamiltonian and $\mathcal{D}(t) = \mathcal{D}_{rel}(t) + \mathcal{D}_{deph}(t)$ is the relaxation tensor describing dissipation processes such as energy relaxation and transfer $(\mathcal{D}_{rel}(t))$ and coherence dephasing $(\mathcal{D}_{deph}(t))$. Energy transfer rates needed for the simulation of the excitation dynamics are taken from Ref. (50), and they are imposed on the model by Lindblad theory(71, 72). We assume that the energy transfer occurs between effective electronic eigenstates, which coincide with spectroscopically observed states. For each pair of electronic states $|n\rangle$ and $|m\rangle$, for which we expect a rate $\gamma_{nm} = \tau_{nm}^{-1}$ of energy transfer from $|m\rangle$ to $|n\rangle$ (note the order of indices in the notation, which is from right to left), we define the Lindblad transfer operator $V_{(nm)}$

 $\sqrt{\gamma_{nm}|n}\langle m|$. The energy transfer part of the relaxation tensor then has the so-called Lindblad form which reads as

$$\mathcal{D}_{rel}(t)\rho(t) = \sum_{(n,m)} V_{(n,m)}\rho(t)V_{(n,m)}^{+} - \frac{1}{2} \{V_{(n,m)}^{+}V_{(n,m)}, \rho(t)\}.$$
 (5)

The sum goes over all pairs of states for which we observe population transfer. The Lindblad operators are purely electronic, which means that during energy transfer from one electronic state to another, the Condon approximation is satisfied – the vibrational wavepacket does not change, only the vibrational potential energy surface (PES) changes "under" the wavepacket. The energy

Science Advances Manuscript Template Page 28 of 70

transfer rates are specified for the downhill energy transfer process, and the energy transfer rate in the opposite direction is set to satisfy the detailed balance condition with a given temperature T

$$\gamma_{mn} = e^{-\frac{E_m - E_n}{k_B T}} \gamma_{nm}. \tag{6}$$

Energy transfer induces dephasing, which is accounted for by corresponding dephasing rates automatically included in the relaxation part of the Lindblad form $\mathcal{D}_{rel}(t)$.

Another source of coherence dephasing are the energy gap fluctuations responsible for the homogeneous linewidth of the features in both absorption and 2DES spectra. We assume for simplicity that absorption spectra have Gaussian lineshapes, which corresponds to a Gaussian linear time dependent response function. A general linear response of a system interacting with the bath of harmonic oscillators is proportional to (see (73))

$$S_n^{(1)}(t) \approx e^{-g_n(t) - i\omega_{ng}t},\tag{7}$$

where $g_n(t)$ is the so-called lineshape function of the transition from the ground state to the excited state $|n\rangle$. In our approximation, the line shape function reads as

$$g_n(t) \approx a_n t^2, \tag{8}$$

where the coefficient a_n is related to the absorption FWHM Δ_n by the relation

$$a_n = \frac{\Delta_n^2}{16ln^2}. (9)$$

In our calculations, we specify the Gaussian FWHM Δ_n for each monomeric molecule n entering the model, and obtain the FWHM Δ_{α} for each transition to the exciton states (the eigenstates of the Hamiltonian), by

$$\Delta_{\alpha} = \sqrt{\sum_{n} |\langle n | \alpha \rangle|^2 \Delta_n^2},\tag{10}$$

where $\langle n|a\rangle$ is a scalar product of the state $|n\rangle$ localized on the molecule a and the state eigenstate $|\alpha\rangle$. The details of Eq. (10) can be found e.g. in Refs. (28, 74). The derivation is based on postulating a pure dephasing operator

$$H_{dp} = \sum_{n} K_{n} = \sum_{n} q_{n} |n\rangle\langle n|, \tag{11}$$

for each electronic state $|n\rangle$, which can be transformed into the eigenstate picture as

$$H_{dp} = \sum_{n} K_{n} = \sum_{\alpha\beta} \sum_{n} \langle \alpha | n \rangle \langle n | \beta \rangle q_{n} | \alpha \rangle \langle \beta | = \sum_{\alpha\beta} q_{\alpha\beta} | \alpha \rangle \langle \beta |. \tag{12}$$

The correlation functions

$$C_{\alpha\alpha}(t) = \langle q_{\alpha\alpha}(t)q_{\alpha\alpha}\rangle, C_{\alpha\beta}(t) = \langle q_{\alpha\alpha}(t)q_{\beta\beta}\rangle, \quad \text{etc.,}$$
 (13)

give rise to excitonic lineshape functions

$$g_{\alpha\alpha}(t) = \int_0^t d\tau \int_0^\tau d\tau' C_{\alpha\alpha}(\tau'), g_{\alpha\beta}(t) = \int_0^t d\tau \int_0^\tau d\tau' C_{\alpha\beta}(\tau'), \text{ etc.}$$
 (14)

which describe optical coherence dephasing and electronic coherence dephasing.

Science Advances Manuscript Template Page 29 of 70

By the same theory, one can also derive the Gaussian decay of the electronic excited state coherence (element of density matrix $\rho_{\alpha\beta}(t)$) as

$$\rho_{\alpha\beta}(t) \approx e^{-g_{\alpha\alpha}(t) - g_{\beta\beta}(t) + 2\text{Re}g_{\alpha\beta}(t)}$$
(15)

which is based on the transformation applied in Eq. (12). The details can be again found in Refs. (28, 74).

2D Electronic Spectra

We express the third order response functions corresponding to the Liouville pathways using the Markovian approximation (neglecting correlation between the time intervals of the non-linear response). The response functions consist in general of the transition dipole moments d of the transitions involved in the pathway, and of the elements of the evolution superoperator G(t), which governs the time evolution of the corresponding reduced density matrix. For instance, for the excited state coherence element $\rho_{nm}(t)$ we have

$$\rho_{nm}(t) = \sum_{kl} G_{nmkl}(t) \rho_{kl}(0). \tag{16}$$

The elements of the superoperator G(t) are obtained by solving Eq. (4) with a special initial condition $\rho_{nm}(0) = \delta_{kn}\delta_{lm}$. From Eq. (16) we can see that under this initial condition we have

$$G_{nmkl}(t) = \rho_{nm}(t). \tag{17}$$

Based on the elements of the superoperator G(t), we can write e.g. rephasing pathways contributing to the SE signal as

$$R_{reph,SE}(t_3, t_2, t_1) = -id_{gn}d_{mg}d_{kg}d_{gl}G_{ngng}(t_3)G_{nmkl}(t_2)G_{glgl}(t_1)$$
(18)

We note that we use the term "pathway" here in places where we should properly write "non-linear response function corresponding to the pathway". This is done for the sake of brevity and it is customary terminology in the theory of non-linear spectroscopy.

All Liouville pathways are constructed in a way similar to Eq. (18). We invoke the so-called secular approximation in the optical coherence intervals (i.e. when one of the elements of the G(t) corresponds to the electronic ground state) so that we assume

$$G_{ngmg}(t) = 0, (19)$$

for $n \neq m$. Crucially, however, we assume no secular approximation for the t_2 interval, and we consider all possible combinations of indices of the evolution superoperator, when concerned with the propagation in the excited state manifold. Non-secular contributions to the t_2 evolution may introduce new peaks into the ω_2 maps, while in the t_1 and t_3 , non-secular effects only lead to small renormalizations of the optical coherence frequencies (see e.g. Olšina et al.(75) for the case of absorption), which can be assumed already included in our modeling.

Simulations of the ω₂ maps

Simulation parameters

The theory described in previous sections is implemented in the spectroscopic package Quantarhei written in Python and available freely in source code form at

http://github.com/tmancal74/quantarhei. The set of Python scripts needed to calculate results presented in the main text and this SI is available at http://github.com/tmancal74/Policht2021a. The set contains the main simulation script and its configuration file, together with several auxiliary scripts to produce figures and movies from the output of the simulations. All files contain description of their usage and installation instructions for the Quantarhei package and related software. The script configuration and input file script Policht2021.yaml summarizes the parameters of the simulations and allows the user to select three different use cases: 1) Single run - the script can calculate ω_2 -maps for a single set of system parameters. In this use case, apart from saving an ω_2 -map of a selected frequency, the script generates details of the vibronic eigenstates of the system, a complete evolution super-operator tensor for a range of t_2 times, as well as snapshots of all Liouville pathways corresponding to the oscillatory signal. 2) Energy gap scan - the script calculates a series of ω_2 -maps for incrementally changing energy gap between the upper exciton state P_{+} of the special pair and the B molecule. The calculated maps can be compiled into a movie demonstrating how the 2D spectrum evolves as a function of the energy gap. 3) Disorder average - the scripts averages ω_2 -maps over a Gaussian energetic disorder of a specified FWHM.

The crucial parameter of the simulation is the location of the vibrational mode within the molecules of the model BRC. Calculations have revealed that the peak patterns consistent with the experimental observation are obtained when the vibrational mode resides on the B molecule. For the rest of the discussion, we will concentrate on this particular case, except for a section in which we demonstrate the incompatibility of the peak patterns obtained from the mode residing on the SP molecules with the experimental data (see section entitled **Vibrational Mode on Special Pair Molecules**).

2D Map Pattern as a Function of Energy Gap

The Supplementary Materials contains the MP4 movies for the vibrational frequencies $\omega = 570 \text{ cm}^{-1}$, 740 cm⁻¹ and 900 cm⁻¹ and for the electronic energy gap ΔE interval (470, 780) cm⁻¹. The file names are found in STable 1. For the frequency $\omega = 740 \text{ cm}^{-1}$, we can clearly observe the transition between this off-resonant situation and the resonant situation when $\Delta E \approx \omega$. At the resonance, the diagonal peak at the excitation frequency of the B molecule is disproportionally enhanced, and the ω_2 –map does not resemble the experimental one.

These movies represent a scan of the electronic energy gap between the upper exciton state P_+ and the eigenstate involving predominantly the B molecule. The energy gap varies between $\Delta E = 470 \text{ cm}^{-1}$ and $\Delta E = 780 \text{ cm}^{-1}$ with a step of 2 cm⁻¹. Black dashed lines represent the position of excitonic transitions, while the red dashed line represents the B exciton energy with a vibrational quantum subtracted. The coincidence of the black and read dashed lines marks the resonance between the electronic and vibrational transitions. The movies demonstrate the changing relative amplitudes of the peak which reflect the changing energy gap, i.e. changing electronic structure. Apart from the energy gaps near the exact resonance, the peaks in the regions 1-4 are mostly clearly visible. At the exact resonance, peaks in the regions 5 and 6 are significantly more enhanced than those in regions 1-4, which cease to be visible. One of the reasons for their disappearance is that their frequency shifts away from the original vibrational frequency.

Disorder Averages

Real molecular systems exhibit energetic disorder. Previous simulations revealed that the amplitude of different peaks in the ω_2 -map depend on the energy gap between the SP and B molecules. Energetic disorder will result in a specific average over the features we observed in the ΔE scan. In simulating spectroscopic signals, it is customary to consider Gaussian energetic disorder for the transition energies of individual molecules in the aggregate, as such a type of disorder seems to best correspond to majority of the experimental situations. We have therefore calculated ω_2 -maps for the three experimentally observed vibrational frequencies considering a Gaussian disorder with the FWHM of 100 cm⁻¹. The results are presented in Figure 5.

Disorder averaged spectra of Figure 5 are the closest to the experimental situation that we can calculate at present. We can see most of the experimentally expected peaks present in the theoretical calculation, with the best correspondence found for the frequency $\omega = 740 \, \mathrm{cm}^{-1}$. There are several systematic sources of discrepancy between our theory and the experiment. Obviously, there is a lack of mutual interaction between the modes in the theoretical calculations, due to the fact that we apply a single mode model only. The absence of the second B molecule in the reduced BRC model is also likely a significant factor. It is also possible that the simple homo-dimer of BChl molecules model of the SP, which we consider, is insufficient, and the expected presence of the charge transfer states in the SP would further influence the details of the spectral features. From the experimental perspective, insufficient spectral bandwidth of the pulses can distort amplitudes of some of the peaks and make thus comparison with the theory based on impulsive (ultrabroad band) excitation less reliable. Nevertheless, the essence of the experimentally observed features, i.e. the presence of peaks at positions 1 to 4 (see the Main Text), is well reproduced by our limited model.

Detailed analysis of the 740 cm⁻¹ mode and excitonic states

The simulations that include the $\omega = 740$ cm⁻¹ mode show spectroscopic patterns most similar to the experimental ones shown in Figure 3 (main text). In Figure 5, we present the ω_2 -map calculated for the parameters of STable 2.

In the 2D spectrum of Figure 5, we select 8 regions which contain peaks visible with a 20 evenly space contours between the maximum of the absolute value of the spectrum and zero. The regions are labeled from 1 to 6 with 1 to 4 representing the locations of the peaks with excitation frequencies on the SP molecules (see the Main Text). The regions 5 and 6 correspond to excitation on the B molecule. We subdivided peaks 1 and 5 into subregions 1a and 1b, and 5a and 5b, respectively, to study separately the two peaks of a double peak structure observed in regions 1 and 5. The border frequencies defining the regions are presented in STable 3. The selected regions each contain a maximum of single spectral peak. We perform a search among all the Liouville pathways corresponding to the ω_2 —map of Figure 5 assign them to individual regions according to their ω_1 and ω_3 frequencies, and order them according to the magnitude of their contribution. A pathway of Eq. (18), characterized by the evolution superoperator element $G_{nmkl}(t_2)$ has a magnitude defined by the product $d_{gn}d_{mg}d_{kg}d_{gl}|G_{nmkl}(t_2)|$ averaged over all possible rotations of the molecule in space. To each peak in the spectrum we can thus assign the most important Liouville pathways and study their properties.

Each pathway is characterized by four optical transitions between electronic eigenstates of the model Hamiltonian, and it is represented by the so-called double sided Feynman diagram(73) listing the order and character of individual perturbations of the system by light. An example of a Liouville pathway is presented in SFigure 9, where we use the textual output of the Quantarhei package directly. The pathway depicted on SFigure 9 is the strongest of the Liouville pathways contributing to the Region 1a. Integer numbers inside the diagram label the Hamiltonian

eigenstates ordered by energy from 0 (the ground state) through the up to double exciton states (e.g. the state 13 on SFigure 9). The diagram describes a sequence of interactions of the system with electric field of the light, with time running from bottom up. The two sides of the diagram correspond to two indices of the density matrix describing the electronic state of the system, with the system always starting in the ground state – as depicted by the two zeros at the bottom of the diagram. Arrows pointing towards the horizontal lines of the diagram depict interactions with the electric field of the light, and it can be noted that after each interaction a state label on the left or right side of the diagram changes. The rules of Feynman diagram representation as explained e.g. in (73) allow us to graphically distinguish between interactions which lead to absorption and emission events, respectively, on the two sites of the diagram. However, our particular rendering of the pathways ignores this additional information. The arrow always points towards the inside of the diagram. The crucial information provided by the diagram are the frequencies of the optical transitions and frequencies of the coherence in the t_2 . This information is presented in the units of cm⁻¹ on the right-hand side of the diagram. The frequency also shows sign which is always negative for the first interval (the first from the bottom frequency) of the rephasing diagrams (which start with an arrow from the right) and positive for the non-rephasing diagrams (which start with an arrow from the left). This particular frequency is optical, i.e. corresponding to absorption of visible light. The second and third frequencies (from the bottom) depict coherences between excited states before and after energy transfer event, which is itself denoted by a horizontal line made of asterisks. If the states before and after the supposed energy transfer event remain the same, the diagram corresponds to the contribution in which the energy transfer does not occur. The frequencies in the excited state correspond either to electronic or vibrational energy gaps. The last frequency depicted in the diagram is again optical, and it corresponds to excited state absorption frequency (in the particular diagram of SFigure 9), because (as will be discussed below) the state 13 is a doubly excited state. Other diagrams might show transitions between the ground state and the excited state in their last interval, corresponding to stimulated emission or ground state bleach signals.

To understand the nature of the different contributions to the 2D spectra as they are revealed by the corresponding Liouville pathways, we need to know the characteristics of the eigenstates of the model Hamiltonian. In particular, the compositions of the single- and double-exciton states of our reduced model of the BRC have to be expressed in terms of the local excited states of the SP and B molecules. In the present Supplementary Materials, we will again use the textual output of the Quantarhei package to our advantage. All eigenstates of the Hamiltonian are ordered by energy (from lowest to highest) and labelled by an integer number starting with 0. For small Huang-Rhys factors, we have verified that only one vibrational excitation is needed in each electronic state in order to obtain reliable results. To ensure convergence of all results, we allow the vibrational mode to be excited to the state with two vibrational quanta both on the ground and excited electronic states of the molecule. The states 0, 1 and 2 of our list therefore correspond to the electronic ground state, with 0, 1 and 2 vibrational quanta. States starting from 3 represent electronically excited states. Quantarhei denotes all these states as "excitons" as they are (strictly speaking) excited states, albeit sometimes of purely vibrational origin.

The output of the Quantarhei package expresses each state composition by a table similar to the one presented in SFigure 9. The meaning of the individual columns in the table is explained in detail in the figure caption of SFigure 9. The information about the eigenstate composition can

be used to understand its physical meaning. First, the second column shows that the state is almost equally composed of two states, namely of the excitations on the two SP molecules. The third column reveals that the state is almost perfectly antisymmetric with respect to the exchange of the molecules in the SP (identities of the excited molecules can be discerned from the fourth column of the table). Moreover, the table shows that the leading states in the composition are not vibrationally excited. The rest of the local states contribute with much less than 1% of the probability of being excited, with about 0.3% probability that the molecule B will be excited, and the probability that the vibrational mode on B is excited smaller by further two orders of magnitude. With such a small contribution from all but the SP states, and with an almost perfect anti-symmetry of the state, the exciton 3 can be identified with the so-call P- state (see e.g. (47)).

In SFigure 10, we present a complete list of single exciton states involved in the analysis of the spectrum in Figure 5. For each state, we present an interpretation of its physical meaning, and an approximate expression in terms of local electronic and vibrational excitation of the SP and B molecules. Single exciton band starts with the exciton 3 (the lowest excited state of BRC – see SFig. 9), which can be approximately described as

$$|P_{-}B_{g0}\rangle = -\frac{1}{\sqrt{2}}(|SP_{1}\rangle|g_{SP_{2}}\rangle - |g_{SP_{1}}\rangle|SP_{2}\rangle)|g_{B}\rangle|\chi_{0}\rangle, \tag{20}$$

where the states $|g_{SP_1}\rangle$ and $|SP_1\rangle$ are the ground state and the excited state of the SP molecule 1, respectively, and similarly for the molecule 2 ($|g_{SP_2}\rangle$ and $|SP_2\rangle$). The state $|g_B\rangle$ is the ground state of the B molecule, and the state $|\chi_n\rangle$ represents the eigenstate of the vibrational mode on the molecule B with n excitations. We skip the exciton state 8 in the SFigure 10, as it does not occur in any of the Liouville pathways discussed below.

Besides the transitions from the ground state to the single exciton states, the 2D spectrum also contains excited state absorption contributions, which involve double-exciton states. Similarly, to SFigure 10, we present all double-exciton states found in the relevant Liouville pathways in SFigure 11. Each state is again represented by a textual output obtained directly from the Quantarhei package in the form of a table listing the involved states, their coefficients in the superposition and state signatures. The double-exciton states are composed of the local excited states of two molecules, as can be readily confirmed by inspecting the occupation number triples of the state signature columns in SFigure 11. The transition energy of the double exciton states and the transition dipole moment are taken from the ground state. This means that the listed transition dipole moment is always zero for the double-exciton states, however, these states have non-zero transition dipole moments from the single-exciton states.

With the details of the Hamiltonian eigenstate properties at hand, as summarized in STable 3, we can attempt a detailed analysis of the Liouville pathways contributing to different regions of the ω_2 -maps, in order to identify interactions and processes behind the individual contributions to the measured spectroscopic signals. We identify four dominant types of coherence processes which we define in the following way:

Type i): decay of vibrational coherence residing in the ground or excited state of the B molecule. In case of the B in the ground state, other states are excited, such as P- in the case of coherence (5,3), so that formally, from the point of view of the collective states of the RC, we deal always with excited state coherence. As the process only involves coherence decay, and it is thus allowed under secular approximation, it is a secular process.

Type ii): vibronic coherence shift from the excited state of B to its ground state accompanied by electronic energy transfer from the B molecule to the P- or P+ states. This process was previously identified by Paleček et al(30) and referred to as ETICS (Energy Transfer-Induced Coherence Shift).

Type iii): electronic to vibrational coherence transfer. These processes involve initially an electronic coherence, such as the one between electronic excited states of the B molecule and the P_{-} state of the SP (e.g. the (6,3) coherence) and transfer into a state characterized by a population of an electronic state (e.g. P_{-}) with a vibrational coherence induced in the ground state of the B molecule. Coherence transfer $(6,3) \rightarrow (5,3)$ is an example of such a process, which can formally be also regarded as a manifestation of ETICS.

Type iv): passive spectator vibrational coherence on B accompanying electronic processes. The process starts either with electronic coherence accompanied by a vibrational coherence in the ground state of B or with an electronic excited state (other than that of the B molecule) and it proceeds towards an electronic state (P+ or P-) accompanied by vibrational coherence in the ground state of the B molecule. The main characteristics of the present process is that the state of the B molecule does not change in its course.

In STable 5, we report the dominant coherence processes exhibited in the ω_2 -maps, listing the states participating in the coherence in the exciton and local state bases. We also classify the process by as Type i-iv and denote where they appear and present this data graphically in Figure 6. STable 5 and Figure 6 neglect any minor pathways contributing less than 10% of the total amplitude of any particular peak. Such minor pathways include type i-iv processes as well as processes such as population-to-coherence transfer.

Region 1a

Regions 1a, 1b and 2 are characterized by the ω_1 excitation frequency corresponding to the exciton 3 of our nomenclature, i.e. to the anti-symmetric delocalized state of the SP, which corresponds to P-, the lowest allowed excited state of the BRC.

The peak in the Region 1a is produced mainly by the four Liouville pathways presented in SFigure 12. The amplitudes AL of the pathways are measured relative to the leading pathway. In the leading pathway $(5,3) \rightarrow (5,3)$ with the relative amplitude $A_L = 1$, the coherence between states 5 and 3 is excited and it decays exponentially (see SFigure 13). The coherence corresponds to a Type i) process, in which the ground state vibrational coherence on the B molecule decays. The states 5 and 3 are nearly identical in their electronic composition, with only an additional vibrational excitation on state B (see SFig. 9 & 10). The corresponding coherence element $G_{5353}(t)$ of the evolution superoperator decays from its initial value of 1 on the time scale of several hundreds of femtoseconds. Its Fourier transform, in SFigure 13, shows a single peak with the maximum at 740 cm-1.

The second most intensive pathway $(6,3) \rightarrow (5,3)$ is a Type iii) process in which an initial coherence is excited between states 6 and 3. The state 6 is predominantly an excitation on the B molecule with a very small contribution from the SP molecule, to which it is directly coupled. The transition dipole moment of the transition from the ground state to state 6 is several orders of

magnitude stronger than that of the transition to state 5, however, the coherence transfer into the coherence (5,3) is weak as we can see by the magnitude of the evolution superoperator element $G_{5363}(t)$ in SFigure 13. This element starts from 0 and peaks at around 200 fs. Its Fourier transform reveals that it oscillates both on the coherence frequency from which it starts, i.e. 1275 cm⁻¹ and the frequency 740 cm⁻¹ of the coherence (5,3).

We can see that the characters of the first two strongest pathways in region 1a are different (Type i) vs Type iii)). Type i) corresponds to a vibrational coherence, which is directly excited in the ground state of the B molecule. Such an excitation is possible due to resonance coupling between transitions involving vibrational quanta and those leaving the vibrational mode unexcited. Such coupling was invoked in Refs. (20, 27) to explain long lived oscillating features in the 2D spectra of the photosynthetic system FMO. The present feature involves excitation of the vibrational quantum in the ground-state of a molecule, and is therefore seemingly related to the version of the mechanism studied in Ref. (20), where ground state vibrations are the ones observed. However, the signal described in Ref. (20) is the ground-state bleach (GSB) signal, and the ground state vibration is reached by stimulating a transition from an excited state to the ground-state by a second of two laser pulse interactions. Here on the contrary, we reach the ground state vibration on the molecule B by one interaction with laser pulse. At the same time, the collective state of the BRC, in which the ground state of B participates, is an excited state. The coherence is therefore formally occurring in the excited state. Type i) pathways such as this correspond to the mechanism of vibronic coherence enhancement proposed in Ref. (27). The second dominant pathway (of Type iii)) corresponds to the mechanism in which the coherence is left behind on a molecule which lost its excitation due to energy transfer. This mechanism was described for the purely vibrational case e.g. in Ref. (76), and it is akin to the energy transfer induced coherence shift (ETICS) mechanism proposed by Paleček, et al. in Ref. (30) with the initial coherence (6,3) being of purely electronic origin. The energy transfer involved here is from the B molecule to the anti-symmetric state P- of the SP. The third strongest Liouville pathway $(7,3) \rightarrow (5,3)$, of Type iv), involves transfer from the coherence between P₊ and P₋ states to the population of the state P₋. During this process the vibrational coherence in the electronic ground state of the B molecule remains largely unaffected.

The fourth pathway $(6,3) \rightarrow (7,4)$, of Type iii), involves an unusual coherence transfer where on both sides of the diagram the states change in an energetic uphill direction. As we work in the eigenstate picture, and the system Hamiltonian does not contribute to coherence transfer, the present feature results from the Lindblad form in the Condon approximation as described above. There is no straightforward interpretation for this particular phenomenon in terms of its contribution to the energy transfer which is minor anyway (similarly to other coherence transfer features). Its importance in the 2D spectrum is enhanced by the fact that some of the states involved in the Liouville pathways are strongly allowed. The Lindblad form guarantees the positivity of the density matrix of the system, and the present contributions to coherence and population transfer, when correctly summed up, are consistent with the density matrix positivity, and with the canonical detailed balance which we impose on the Lindblad theory in the present work.

It is also important to state that we describe the features of the Liouville pathways and the states involved in them by their leading contributions. Sometimes, however, minor contributions of other states may have decisive role in determining their characters, too. For instance, when the state 5 is concerned, its leading character predicts transition dipole moment from the ground state equal to zero. Only the small contributions (below 1% of the probability) of the states involving

the B molecule give it an allowed character. It is entirely possible, that in some minor contributions to the spectra, the processes that are actually significant, proceed between the local states, which are not included in our characterization of the eigenstates.

Regions 1b and 2

The Liouville pathways contributing to the region 1b (SFig. 14A) are very similar to those of the region 1a, except for different two-exciton states in the ESA. Involvement of a different two-exciton state leads to different spectral position of the peak on the ω_3 axis. While in region 1a the final ultrashort excitation occurs on the B molecule, the final excitation in region 1b goes to state 14 and corresponds to the transition from one of the SP delocalized states, to the SP double exciton state. All relevant coherence evolutions are already presented in SFigure 13. The leading pathway corresponds to a decay of the ground state vibrational coherence on the molecule B (Type i)), the other two contributions represent electronic to vibrational coherence transfer $(6,3) \rightarrow (5,3)$ of Type ii and the coherence transfer $(7,3) \rightarrow (5,3)$ which is of Type iii).

The region 2 (SFig. 14B) shows similar character to region 1b, displaying a dominant pathway of Type i, as well as contributions from Types iii) and iv). The main difference is again the final two-exciton state of the Liouville pathways. The final excitation of these pathways occurs again on the B molecule, but involves also an additional vibrational quantum in the excited state of B.

Regions 3 and 4

Regions 3 (SFig. 14C) and 4 (SFig. 14D) are characterized by the ω_1 frequency corresponding to the transition from the ground state to the state 4 of our nomenclature, and thus correspond to the position of the elusive P+ state of the SP. The final transition of the Liouville pathways goes into the state 13, which means that it occurs on the B molecule. Both leading pathways ((7,4) \rightarrow (5,3) and (6,4) \rightarrow (5,3)) have similar magnitude and involve coherence transfer to (5,3), which played a major role in the regions 1a, 1b and 2, and which corresponds predominantly to the vibrational coherence in the ground state of the B molecule, while the electronic state P- is excited. The starting coherence corresponds to the same vibrational coherence on the B molecule, however, now with the P+ molecule excited. The vibrational coherence is thus riding here on the P+ to P- energy transfer. In the second, slightly less intensive contribution, the coherence transfer starts from (6,4), an electronic coherence between the B molecule and the P+ state. This particular coherence transfer thus follows from both P+ to P- and B to P- energy transfer processes. The time evolutions of these coherence processes are shown in SFigure 15.

Region 4 starts with the state 4, just as the region 3, but finishes with the transition from P-state to the doubly excited state 16. This transition corresponds to the excitation of the B molecule to the vibrationally (one quantum) excited electronic excited state. The relative amplitude of the two contributions are necessarily similar as in region 3, and the discussion of the coherence transfer in region 3 applies to the region 4 as well.

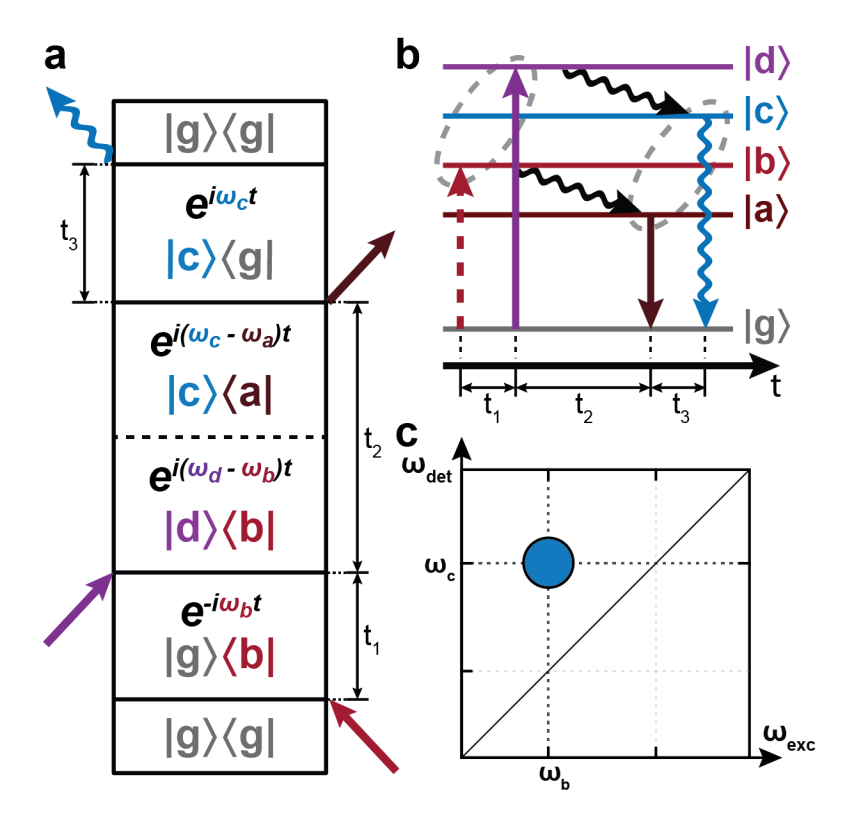
Regions 5a, 5b and 6

With regions 5a, 5b and 6 (SFig, 16) we arrive at the excitation frequency of the B molecule. All the pathways in these regions start with the excitation to the state 6, which corresponds to the 0-0 transition on the B molecule. Second excitation always occurs into the state 9, representing the vibrationally excited electronic excited state of the B molecule. The initial coherence (9, 6) in these regions is thus always the excited state vibrational coherence on the B molecule. One of the leading pathways in all three regions (the second strongest in 5a, and

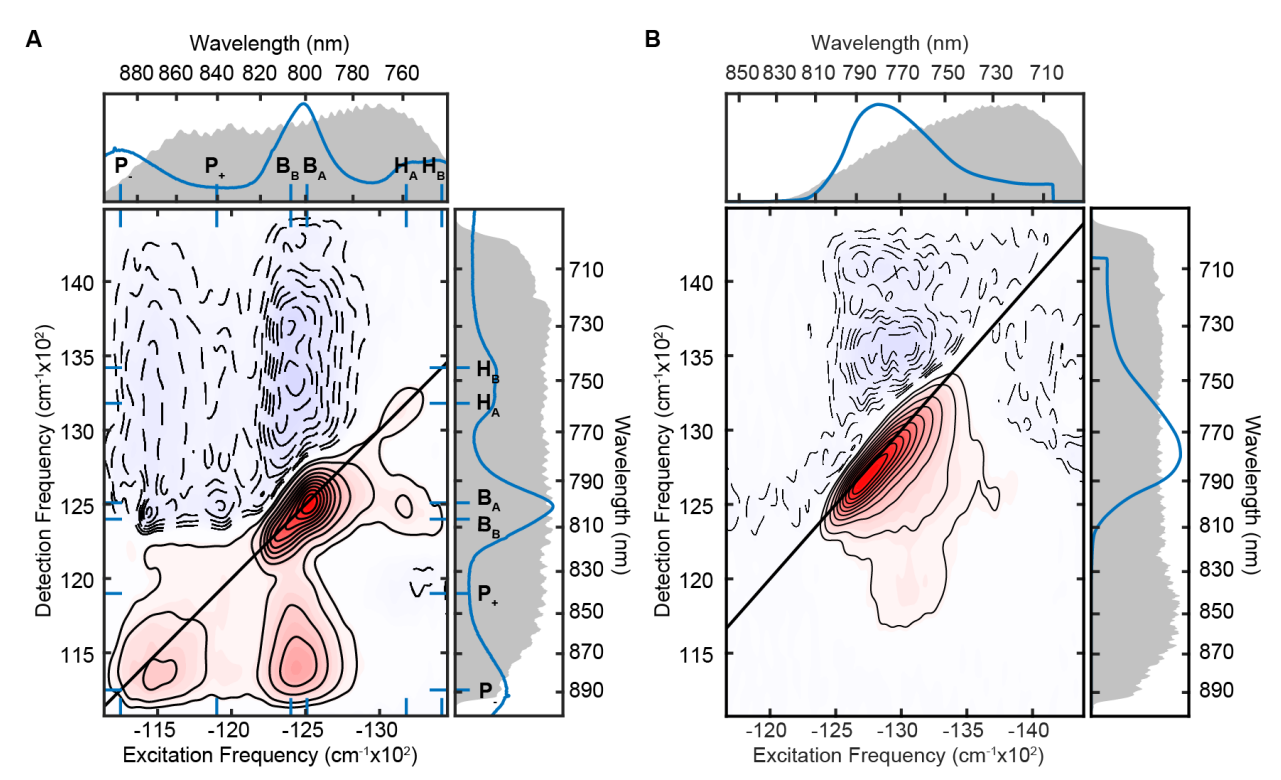
5b and the strongest in region 6) corresponds to the decay of this excited state coherence, which occurs with the time constant driven by the energy transfer away from the B molecule (Type i) coherence). By necessity, depopulation of the excited state of B is accompanied by shifting the vibrational coherence from its electronically excited state to its electronic ground state. This shift is expressed in other two coherence transfer processes contributing in this spectral region, namely coherence transfers $(9,6) \rightarrow (5,3)$ and $(9,6) \rightarrow (7,4)$ accompanying the B to P- and B to P+ energy transfer, respectively. All the coherence transfer pathways in these regions therefore correspond to the ETICS process (Type ii)) in which the vibrational wavepacket (coherence) in the excited state of the B molecules is "shifted" to the ground state of the B molecule due to the excitation transferring to the P+ or P- states. Unlike all other pathways considered here, which are of the excited state absorption (ESA) type, the excited state vibrational coherence decay pathways in regions 5a and 6 are of the stimulated emission (SE) type, and carry the opposite sign (or a 180° phase shift) with respect to most other contributions. We can expect partial cancellation of the contributions these two regions. The evolution of coherences involved in the ω_2 -maps in the regions 5a, 5b and 6 is presented in SFigure 17.

Vibrational Mode on Special Pair Molecules

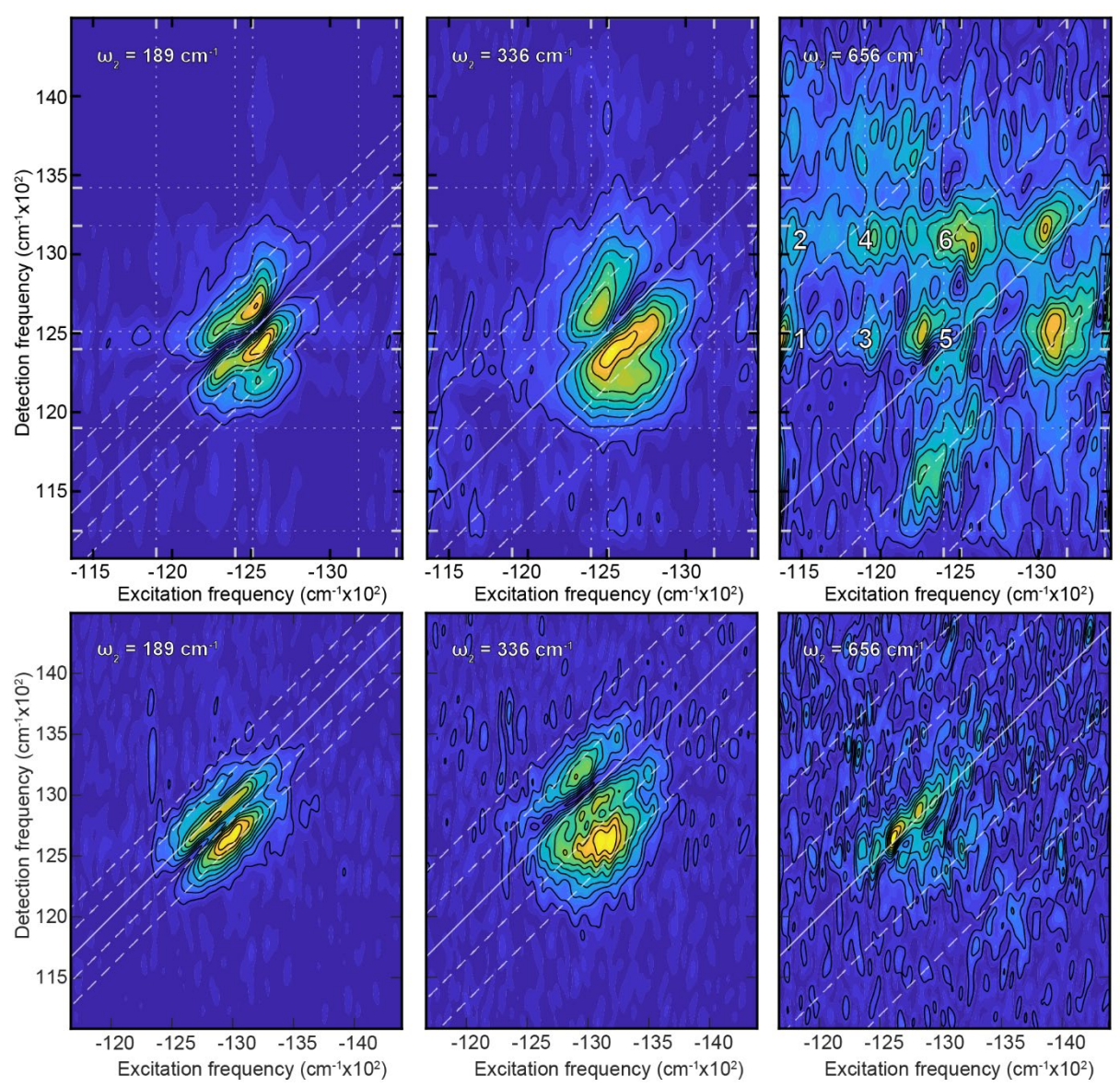
In this section we demonstrate that placing the vibrational mode on one of the SP molecules leads to a peak pattern, which is clearly not compatible with the experimental observations. We present all four types of ω_2 maps, which we can construct from our simulations, in SFigure 18. These figures clearly show that the experimentally observed patterns change their position between the different types of signals (rephasing vs. non-rephasing and positive vs. negative frequencies) in the same way as the theoretical patterns obtained when the vibrational mode is placed on the B molecule. The patterns produced in our simulations with the vibrational mode assigned to one of the SP molecules appear largely outside the experimentally observed spectral window, and they do not contribute to the region where we observe interesting signals. We can therefore exclude the possibility that the experimentally observed signal originates from vibrational modes of the special pair molecules.



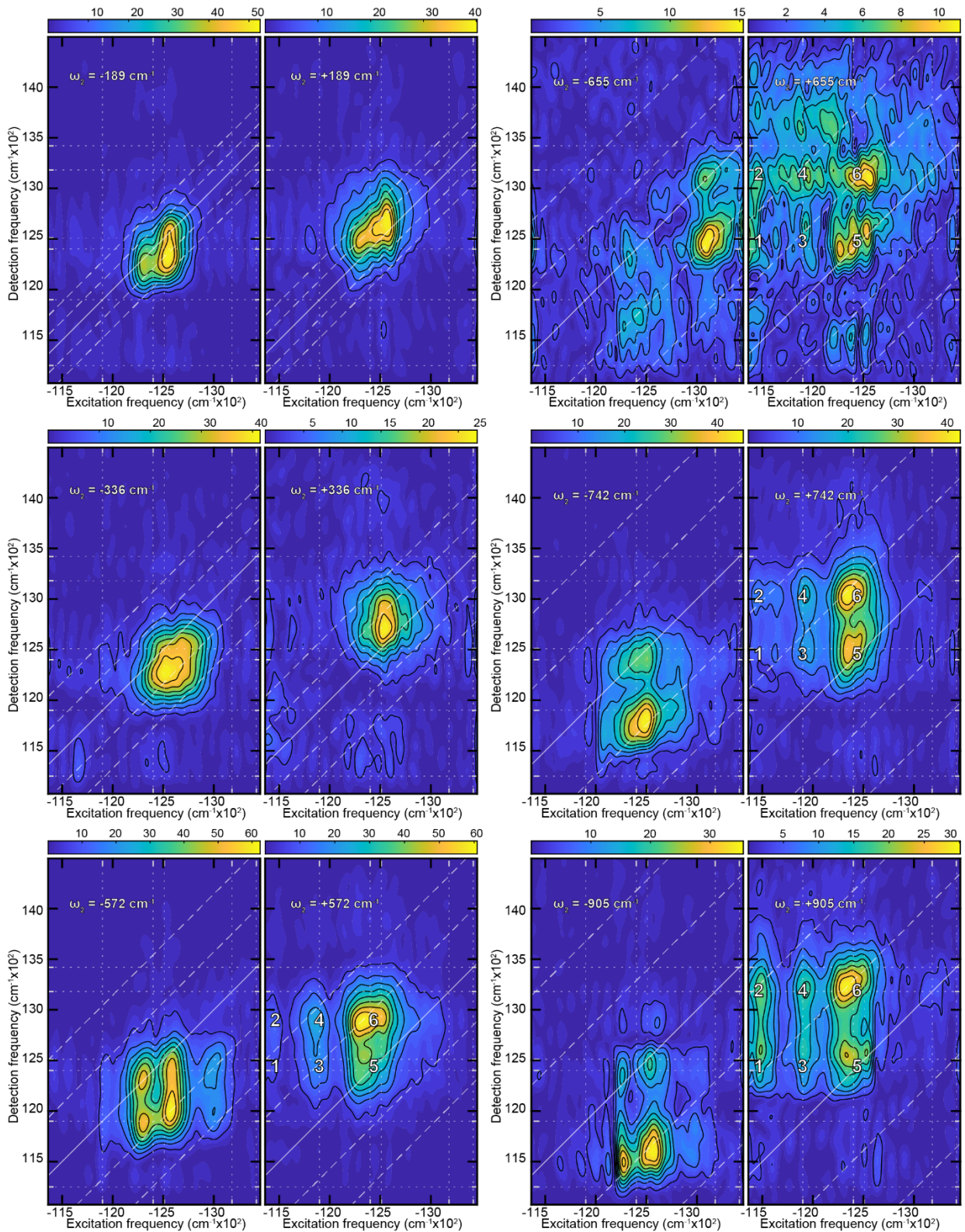
SFig. 1 (**A**) Rephasing Double-sided Feynman diagram for a stimulated emission signal involving coherence transfer from the state pair $|d\rangle\langle b|$ to a state pair $|c\rangle\langle a|$. Straight arrows denote actions of the laser pulse causing transitions between the ground state and the excited states depicted in section (**B**). Colors correspond to the involved excited states. The last wavy arrow corresponds to the emitted signal. (**B**) States involved in the Feynman diagram and the corresponding action of the pulses. The first pulse excites the system into the state $|b\rangle$, while the second interaction excites state $|d\rangle$. The resulting density matrix element probed by this Liouville pathways is the coherence $|d\rangle\langle b|$, which changes into coherence $|c\rangle\langle a|$ during the interval t_2 . The third pulse stimulate the transition from state $|a\rangle$ to the ground state and the signal produced corresponds to emission from state $|c\rangle$. (**C**) Cartoon 2D map showing the spectral position of the signal described by pathways in (**A**) and (**B**).



SFig. 2 2D Real Absorptive signal of W(M250)V BRC (**A**) and monomeric Bacteriochlorophyll a in isopropanol (**B**) at t2 = 200 fs and 77 K. Pump and probe spectra (top and right panels, respectively) are shown in grey with the 77 K linear absorption spectrum for BChl.

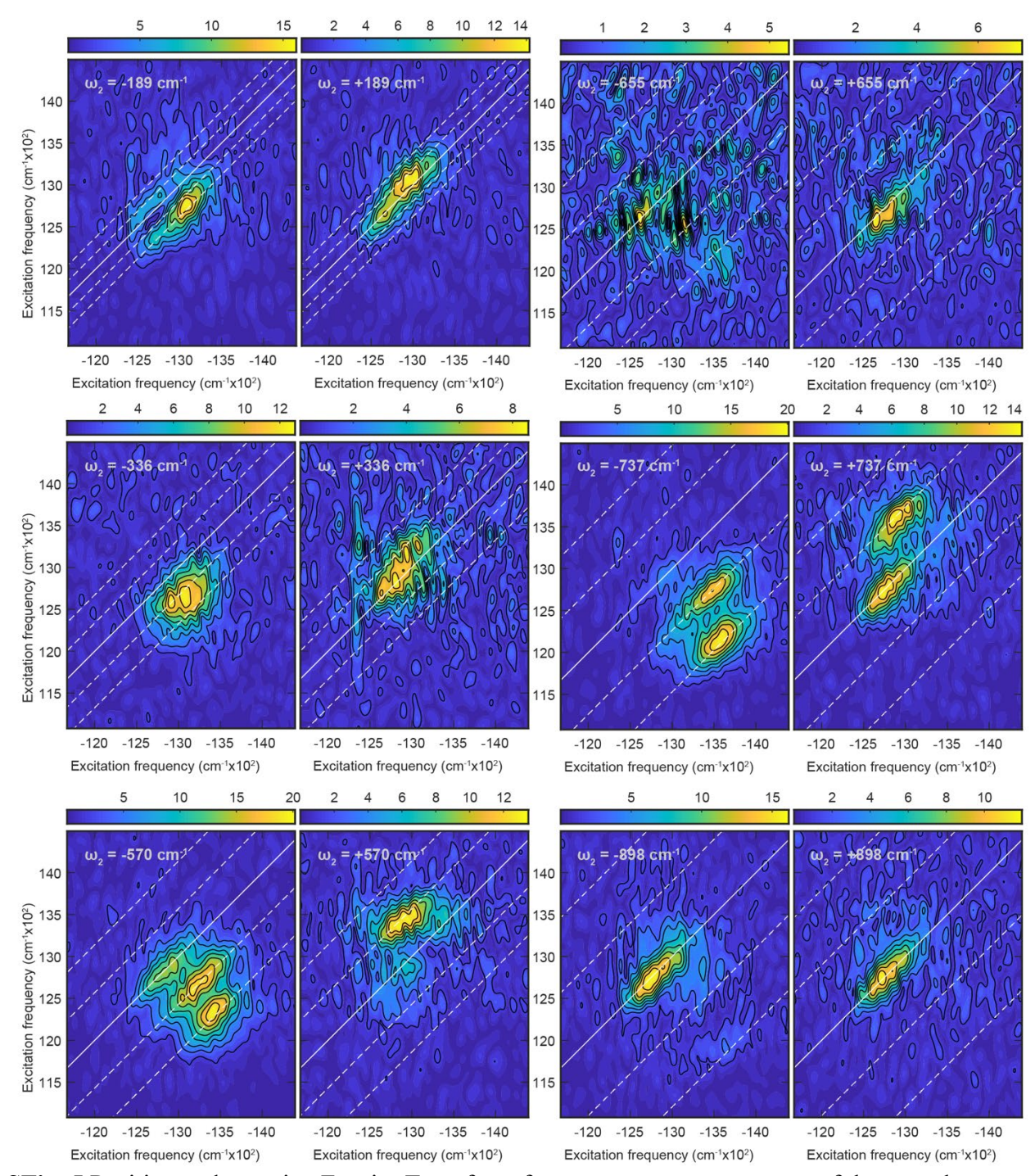


SFig. 3 Additional Coherence Maps for the BRC (top row) and BChl (bottom row) derived from the real rephasing 2D spectra. Maps are shown for prominent low frequency modes $\omega_2 \approx 200 \text{ cm}^{-1}$ (left column) and 340 cm⁻¹ (center column) and low-amplitude mode $\omega_2 \approx 655 \text{ cm}^{-1}$ (right column).

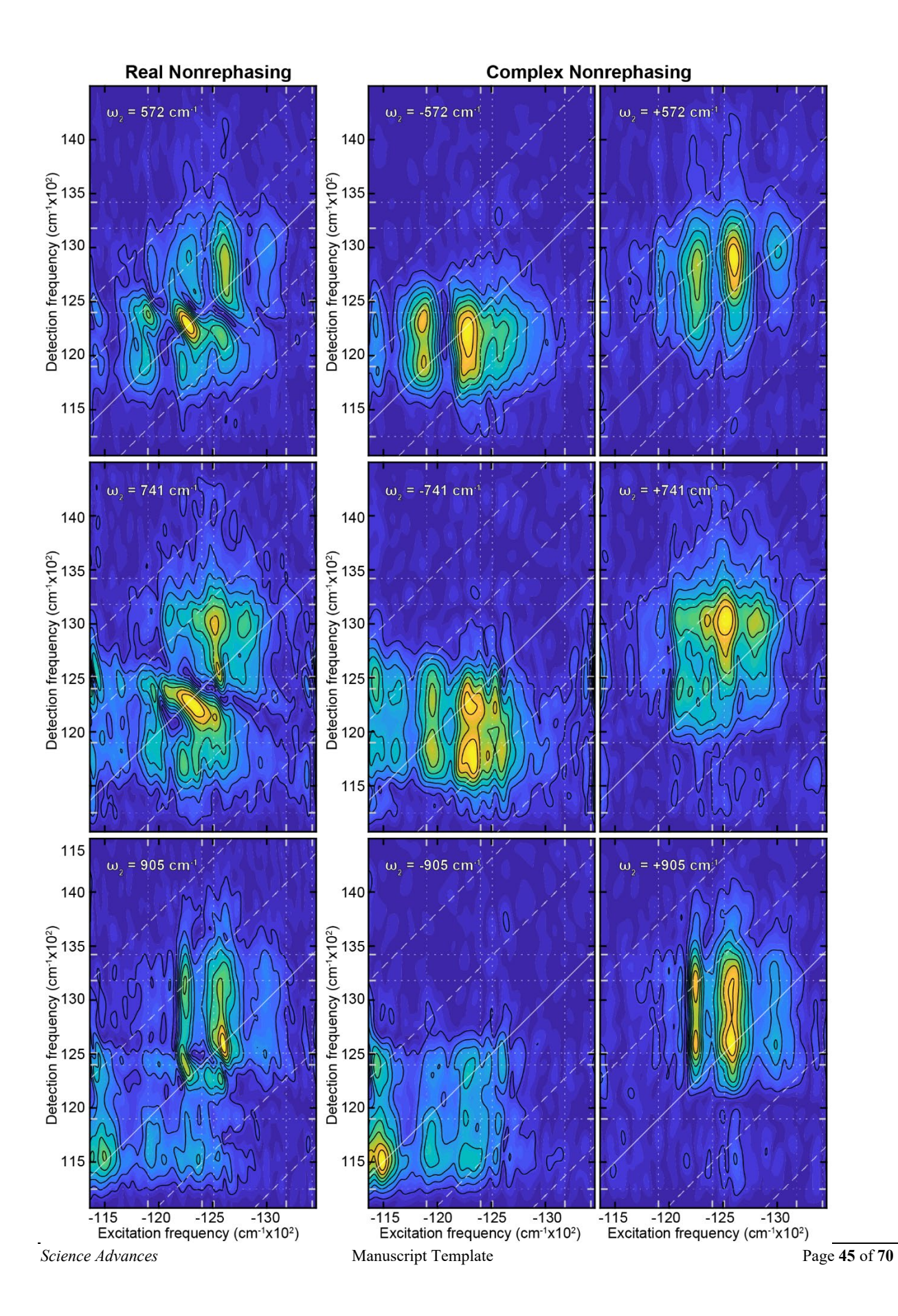


SFig. 4 Positive and negative Fourier Transform frequency component maps of the complex rephasing signal of the BRC. The corresponding real rephasing maps for modes 572, 742, and 905 cm⁻¹ are presented in Figure 3 and for modes 189, 336, and 656 cm⁻¹ in SFigure 3. For each

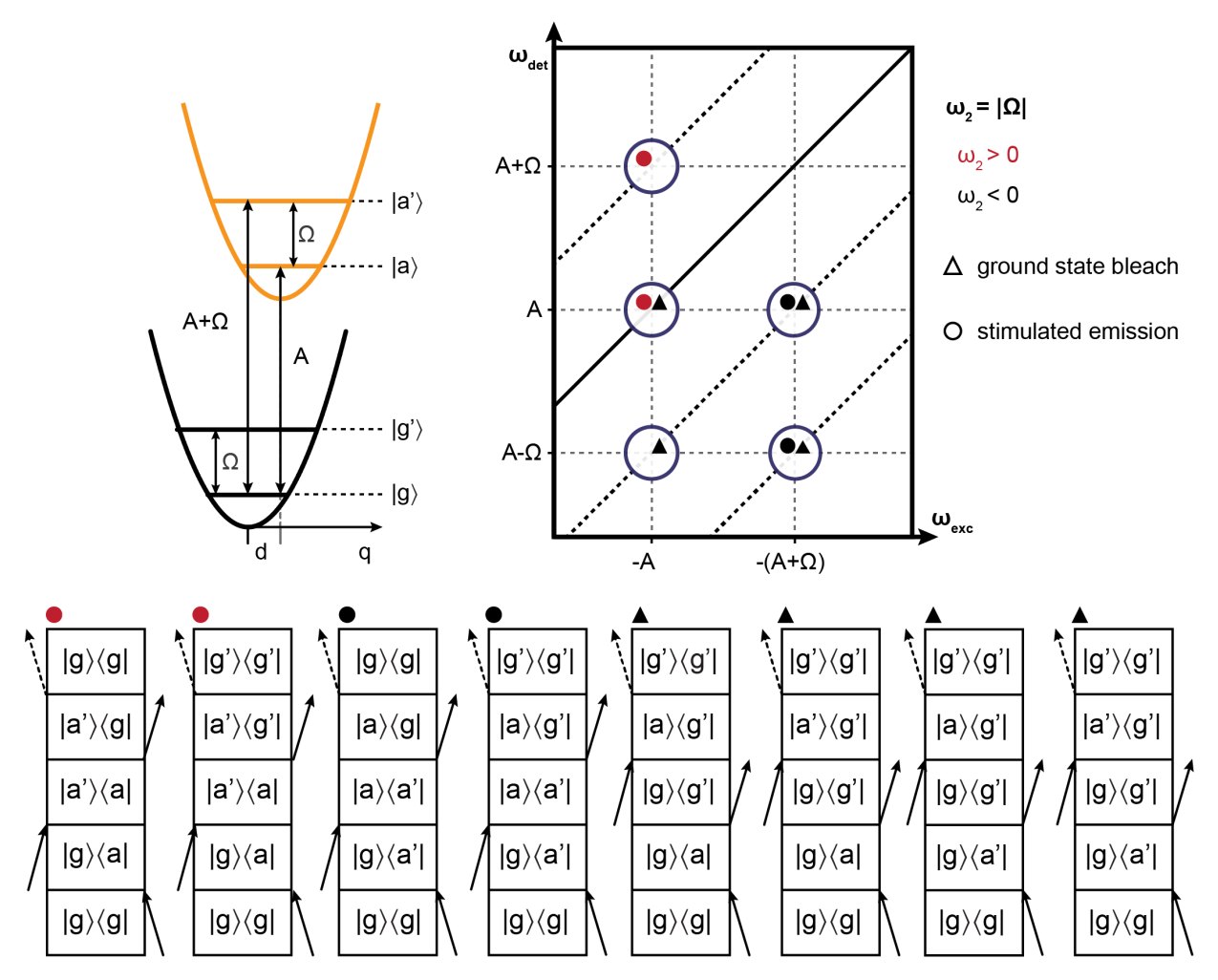
map, the diagonal ($\omega_{exc} = \omega_{det}$) is indicated by a solid diagonal line and parallel dashed white lines are offset from the diagonal by $\pm \omega_2$ and $-2\omega_2$ to aid in their interpretation. BRC excitonic energies taken from Niedringhaus, et.al.(50) are indicated by white dotted vertical and horizontal lines.



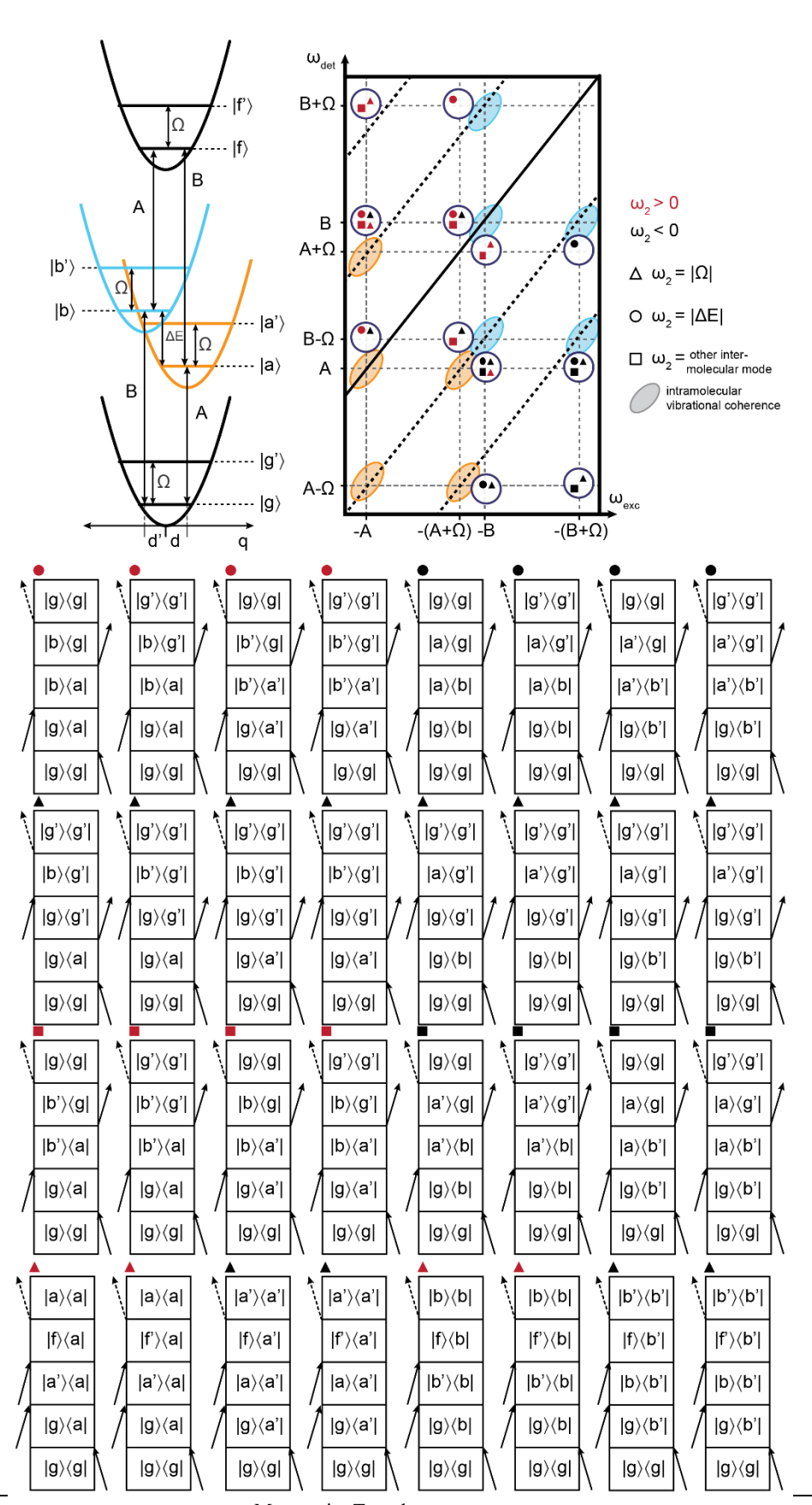
SFig. 5 Positive and negative Fourier Transform frequency component maps of the complex rephasing signal of BChl in isopropanol. The corresponding real rephasing maps for modes 572, 742, and 905 cm⁻¹ are presented in Fig. 3 and for modes 189, 336, and 656 cm⁻¹ in SFigure 3 For each map, the diagonal ($\omega_{\text{exc}} = \omega_{\text{det}}$) is indicated by a solid diagonal line and parallel dashed white lines are offset from the diagonal by $\pm \omega_2$ and $-2\omega_2$ to aid in their interpretation.



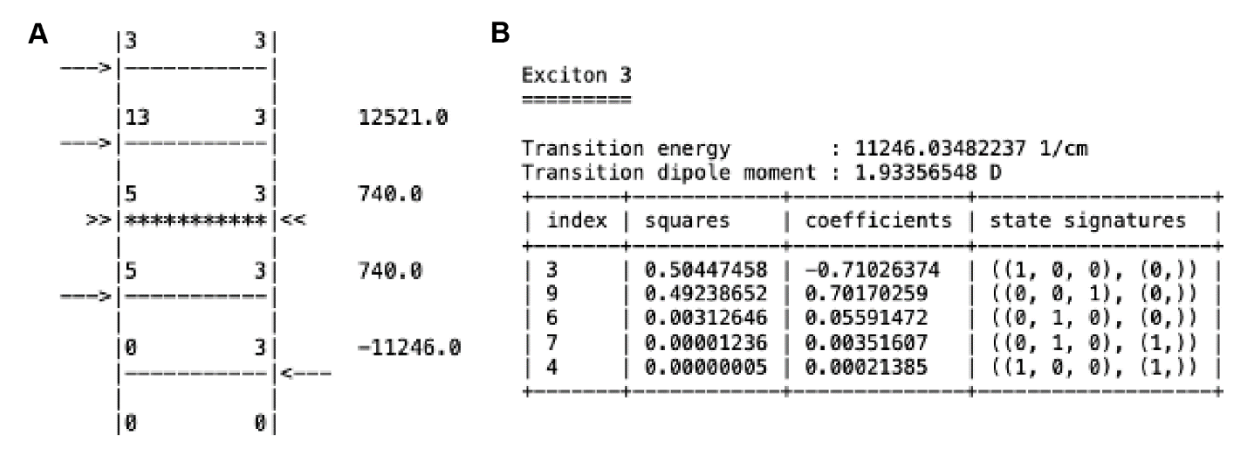
SFig. 6 Real and complex nonrephasing coherence maps for BRC. Maps are shown for ω_2 values of 572 cm⁻¹, 741 cm⁻¹ and 905 cm⁻¹. For each map, the diagonal ($\omega_{exc} = \omega_{det}$) is indicated by a solid diagonal line and parallel dashed white lines are offset from the diagonal by $\pm \omega_2$ and $-2\omega_2$ to aid in their interpretation. BRC excitonic energies taken from Niedringhaus, et.al.(50) are indicated by white dotted vertical and horizontal lines



SFig. 7 Model of purely vibrational coherence. (Top, left) A Jablonski diagram of the displaced harmonic oscillator with 4 states. (Top,right) The expected signal distribution in a 2D coherence map at $\omega_2 = |\Omega|$ features a characteristic "chair"-like distribution. (Bottom) All 8 possible rephasing light-matter interactions which give rise to the coherence signals in the 2D coherence map depicted as Double-sided Feynman diagrams(7, 34, 55, 69).



SFig. 8 Model of mixed electronic-vibrational or vibronic coherence. (Top, left) A Jablonski diagram of all possible electronic states including two singly-excited manifolds (blue and orange) and one doubly-excited manifold (black, $|f\rangle$, $|f\rangle$) for a system where the electronic energy gap is larger than the vibrational mode Ω . (Top, right) Resulting 2D coherence signal distribution for several characteristic coherence frequencies, coded by shape(20, 27, 35).



SFig. 9 (A) The strongest Liouville pathway of the region 1a of the spectrum from Figure 6. (B) Properties and composition of the Exciton 3 as revealed by the output from the Quantarhei package. Transition energy of the state from the ground state is depicted in the units of cm⁻¹ and the transition dipole moment strength of the transition from the ground state is depicted in Debyes. The table contains a list the local states (states defined on individual molecules) participating in this eigenstate of the Hamiltonian. First column lists the indices of the local states involved, the second column lists the squares of the exciton expansion coefficients in terms of the local states, third column lists the exciton expansion coefficients themselves. The last column depicts the excitations of the molecules composing the aggregate (a triple of numbers) and of the vibrational mode (a single number) respectively, in terms of their "occupation numbers". The number 1 means that the corresponding molecule or vibrational mode is excited to its first excited state level (in the case of vibrational modes, the occupation number can be larger that 1). The meaning of the positions in the triple is given by the order in which the molecules are added to the model aggregate in the script, and in the present SI the first and the third positions correspond the SP molecules, while the middle position depicts the B molecule. Thus, the first row shows that exciton 3 corresponds to the 50 % probability of the excitation being on the local state with index 3 (as discerned from the value of 0.50 of the square of the expansion coefficient) and this local state corresponds to the excitation of one of the SP molecules (as discerned from the number 1 in the first position of the triple). At the same time, the vibrational mode residing in the molecule B is not excited in the exciton state 3.

Exciton 4

Transition energy : 11892.05002672 1/cm Transition dipole moment : 0.15471905 D

index	squares	coefficients	state signatures
9	0.50595414	0.71130454	((0, 0, 1), (0,))
3	0.48150414	0.69390499	((1, 0, 0), (0,))
6	0.01249710	-0.11179043	((0, 1, 0), (0,))
7	0.00002322	-0.00481833	((0, 1, 0), (1,))
4	0.00001343	-0.00366455	((1, 0, 0), (1,))

$$\begin{aligned} &|P_{+}B_{g0}\rangle \\ &= \frac{1}{\sqrt{2}}(|SP_{1}\rangle|g_{SP_{2}}\rangle \\ &+ |g_{SP_{1}}\rangle|SP_{2}\rangle)|g_{B}\rangle|\chi_{0}\rangle, \end{aligned}$$

Exciton 5

Transition energy : 11985.99734064 1/cm Transition dipole moment : 0.00006240 D

index	squares	coefficients	state signatures
4	0.50445704		((1, 0, 0), (1,))
10	0.49225722		((0, 0, 1), (1,))
7	0.00306812		((0, 1, 0), (1,))
6	0.00015933		((0, 1, 0), (0,))
8	0.00002449		((0, 1, 0), (2,))

$$\begin{aligned} & \left| P_{-}B_{g1} \right\rangle \\ &= -\frac{1}{\sqrt{2}} (|SP_{1}\rangle|g_{SP_{2}}\rangle \\ &- |g_{SP_{1}}\rangle|SP_{2}\rangle)|g_{B}\rangle|\chi_{1}\rangle, \end{aligned}$$

Exciton 7

Transition energy : 12632.60830549 1/cm Transition dipole moment : 0.00497380 D

index	squares	coefficients	state signatures
10	0.50317205	-0.70934622	((0, 0, 1), (1,))
4	0.48054437	-0.69321308	((1, 0, 0), (1,))
7	0.01223043	0.11059126	((0, 1, 0), (1,))
6	0.00390500	0.06249003	((0, 1, 0), (0,))
3	0.00005846	0.00764617	((1, 0, 0), (0,))

$$|B_{e0}\rangle = (0.99|g_{SP_1}\rangle|g_{SP_2}\rangle|B\rangle + 0.12|SP_1\rangle|g_{SP_2}\rangle|g_B\rangle)|\chi_0\rangle \approx |g_{SP_1}\rangle|g_{SP_2}\rangle|B\rangle|\chi_0\rangle$$

Exciton 6

Transition energy : 12521.50382878 1/cm Transition dipole moment : 0.89744706 D

tt					
index	squares	coefficients	state signatures		
6 3 10 9	0.98030648 0.01390550 0.00292203 0.00163949 0.00117971	0.99010427 0.11792157 0.05405581 0.04049060 0.03434687	((0, 1, 0), (0,)) ((1, 0, 0), (0,)) ((0, 0, 1), (1,)) ((0, 0, 1), (0,)) ((1, 0, 0), (1,))		

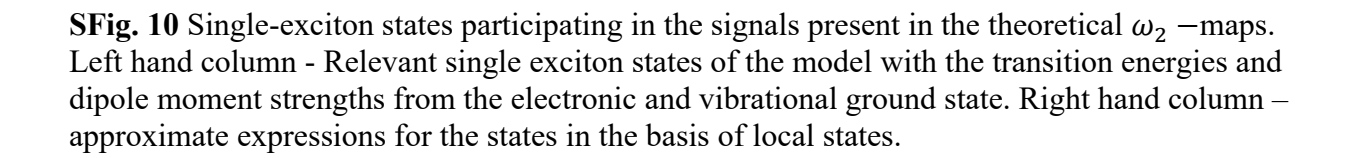
$$\begin{aligned} & \left| P_{+}B_{g1} \right\rangle \\ &= -\frac{1}{\sqrt{2}} (|SP_{1}\rangle|g_{SP_{2}}\rangle \\ &+ |g_{SP_{1}}\rangle|SP_{2}\rangle)|g_{B}\rangle|\chi_{1}\rangle, \end{aligned}$$

Exciton 9

Transition energy : 13260.99891142 1/cm Transition dipole moment : 0.00897201 D

index	squares	coefficients	state signatures
7	0.97670954	0.98828616	((0, 1, 0), (1,))
4	0.01358263	0.11654453	((1, 0, 0), (1,))
11	0.00570140	0.07550763	((0, 0, 1), (2,))
5	0.00229058	0.04785997	((1, 0, 0), (2,))
10	0.00160313	0.04003913	((0, 0, 1), (1,))

$$\begin{aligned} &|B_{e1}\rangle\\ &= (0.99 |g_{SP_1}\rangle |g_{SP_2}\rangle |B\rangle\\ &+ 0.12 |SP_1\rangle |g_{SP_2}\rangle |g_B\rangle) |\chi_1\rangle\\ &\approx |g_{SP_1}\rangle |g_{SP_2}\rangle |B\rangle |\chi_1\rangle \end{aligned}$$



Exciton 13

Transition energy : 23767.471676 Transition dipole moment : 0.00000000 D : 23767.47167611 1/cm

index	squares	coefficients	state signatures
12	0.50323162	-0.70938820	((1, 1, 0), (0,))
18	0.48035923	0.69307953	((0, 1, 1), (0,))
15	0.01244608	0.11156201	((1, 0, 1), (0,))
16	0.00389932	0.06244451	((1, 0, 1), (1,))
19	0.00005763	-0.00759157	((0, 1, 1), (1,))

$$\begin{split} &|P_{-}\rangle|B_{e0}\rangle\\ &=\frac{1}{\sqrt{2}}(-|SP_{1}\rangle|g_{SP2}\rangle\\ &+|g_{SP1}\rangle|SP_{2}\rangle)|B_{e}\rangle|\chi_{0}\rangle \end{split}$$

Exciton 14

Transition energy : 23878.60681665 1/cm Transition dipole moment : 0.00000000 D

1				
į	index	squares	coefficients	state signatures
	16 19 12 13 18	0.98053863 0.01364003 0.00292002 0.00160857 0.00117763	-0.99022151 0.11679056 -0.05403725 -0.04010694 0.03431668	((1, 0, 1), (1,)) ((0, 1, 1), (1,)) ((1, 1, 0), (0,)) ((1, 1, 0), (1,)) ((0, 1, 1), (0,))

$$|2SP_{\gamma}|B_{g1}\rangle = |SP_{1}\gamma|SP_{2}\gamma|B_{g}\gamma|\chi_{1}\rangle$$

Exciton 15

Transition energy : 24414.03098039 1/cm Transition dipole moment : 0.00000000 D

index squares coefficients state signatures 18		4	L	L
12	index	squares	coefficients	state signatures
	12 15 16	0.49219486 0.00312978 0.00016054	-0.70156600 -0.05594440 0.01267054	((1, 1, 0), (0,)) ((1, 0, 1), (0,)) ((1, 0, 1), (1,))

$$\begin{aligned}
&-|P_{+}\rangle|^{B_{e0}}\rangle \\
&= -\frac{1}{\sqrt{2}}(|SP_{1}\rangle|g_{SP_{2}}\rangle \\
&+ |g_{SP_{1}}\rangle|SP_{2}\rangle)|B_{e}\rangle|\chi_{0}\rangle
\end{aligned}$$

Exciton 16

Transition energy : 24506.929798.
Transition dipole moment : 0.00000000 D : 24506.92979830 1/cm

index squares coefficients state signature	s
1 ===== 1 =============================	
13))))))

$$\begin{aligned} &-|P_{-}\rangle|B_{e1}\rangle \\ &= -\frac{1}{\sqrt{2}}(|SP_{1}\rangle|g_{SP_{2}}\rangle \\ &-|g_{SP_{1}}\rangle|SP_{2}\rangle)|B_{e}\rangle|\chi_{1}\rangle \end{aligned}$$

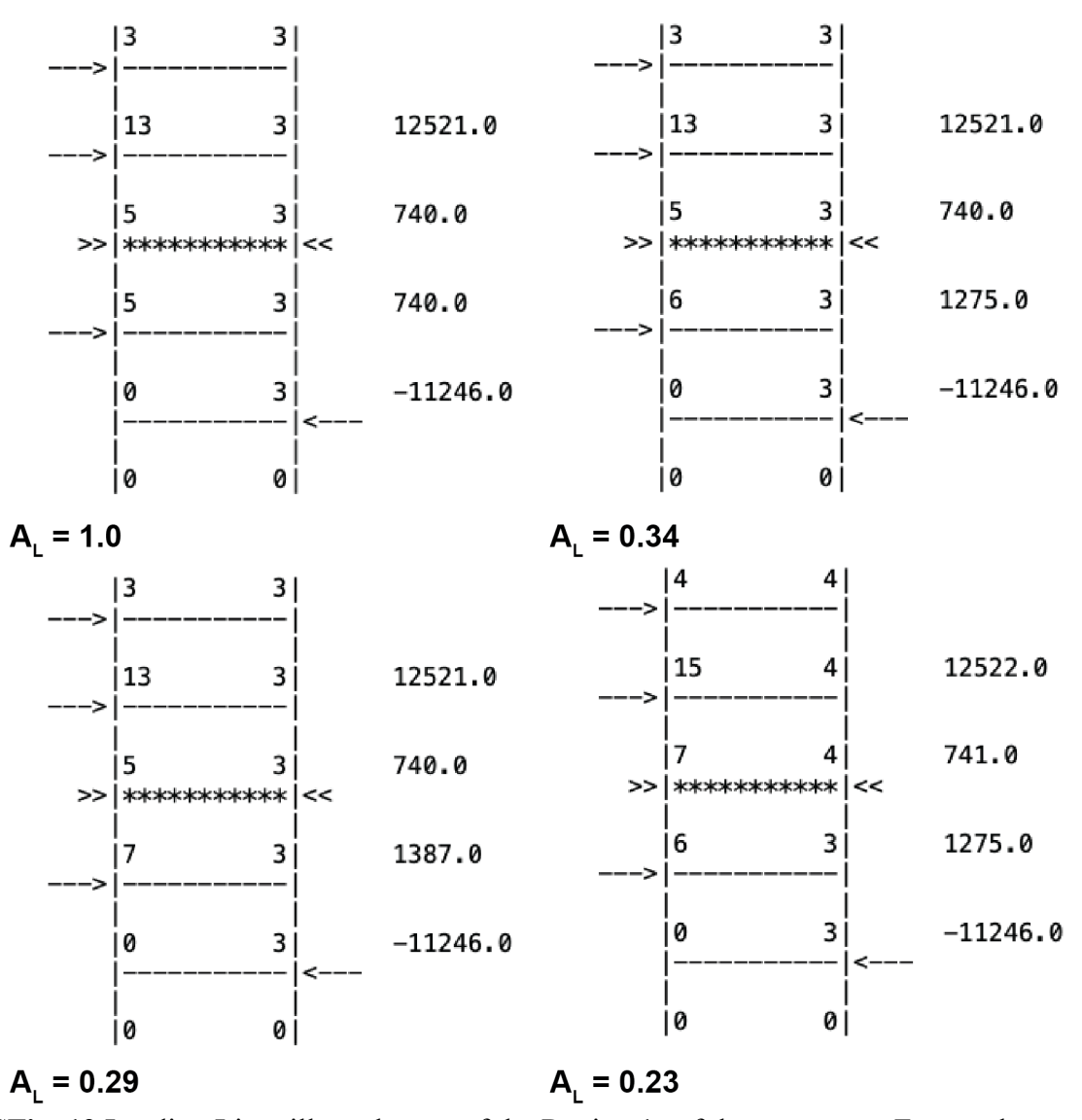
Exciton 18

Transition energy Transition dipole moment : 0.00000000 D

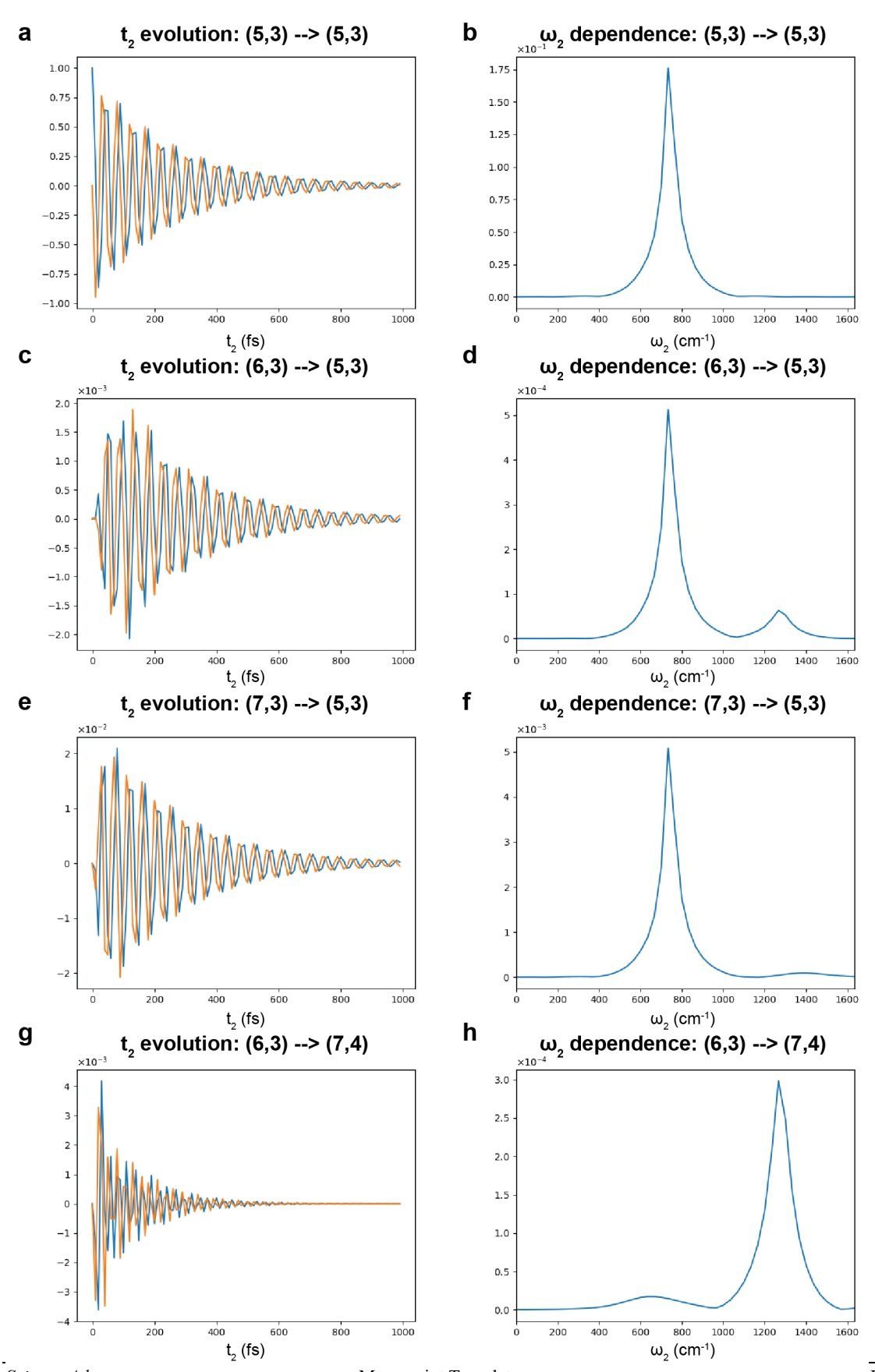
index	squares	coefficients	state signatures
19	0.50446635		((0, 1, 1), (1,))
13	0.49206934		((1, 1, 0), (1,))
16	0.00307134		((1, 0, 1), (1,))
17	0.00031742		((1, 0, 1), (2,))
20	0.00003883		((0, 1, 1), (2,))

$$\begin{split} &|P_{+}\rangle|B_{e1}\rangle\\ &=\frac{1}{\sqrt{2}}\big(|SP_{1}\rangle\big|g_{SP_{2}}\rangle\\ &+|g_{SP_{1}}\rangle|SP_{2}\rangle\big)|B_{e}\rangle|\chi_{1}\rangle \end{split}$$

SFig. 11 Two-exciton states participating in the signals present in the theoretical ω_2 -maps. Two-exciton states consists of states involving two excitations residing simultaneously on two different molecules of the aggregate. The tables list the transition dipole moments for the transition from the ground state and correspondingly all listed values are equal to zero.

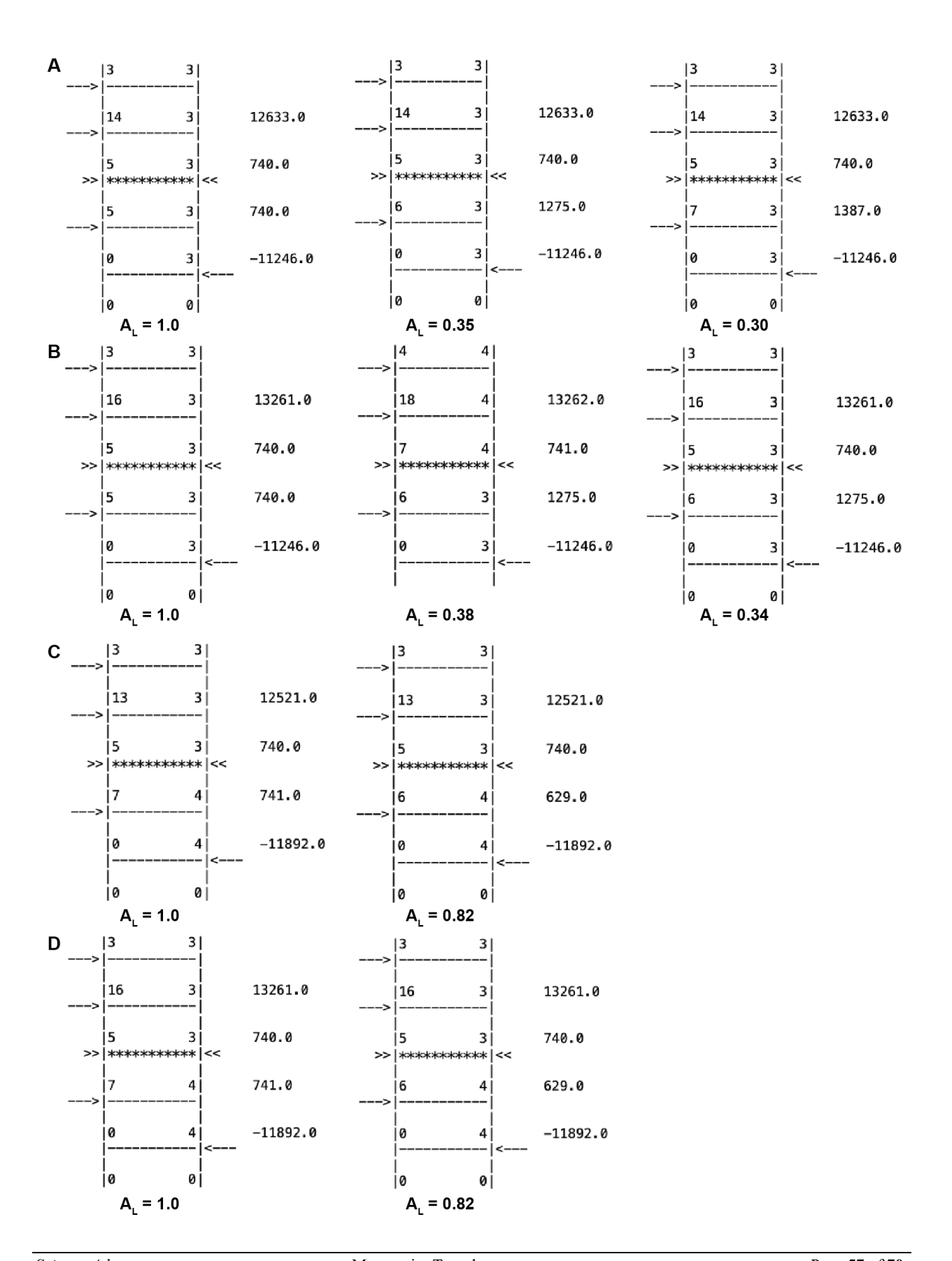


SFig. 12 Leading Liouville pathways of the Region 1a of the ω_2 -map. Four pathways, listed from left to right and from top down, have relative amplitudes AL (listed with each pathway) larger than 10%.

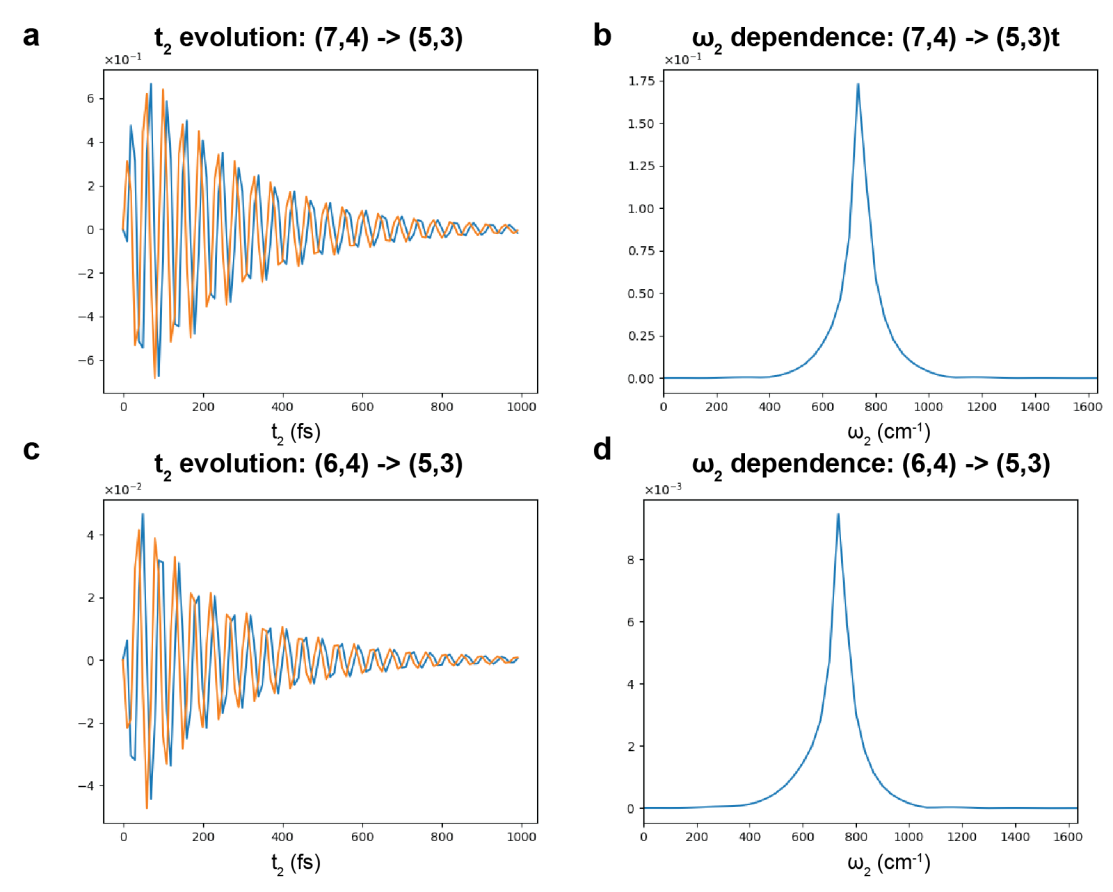


Science Advances Manuscript Template Page 55 of 70

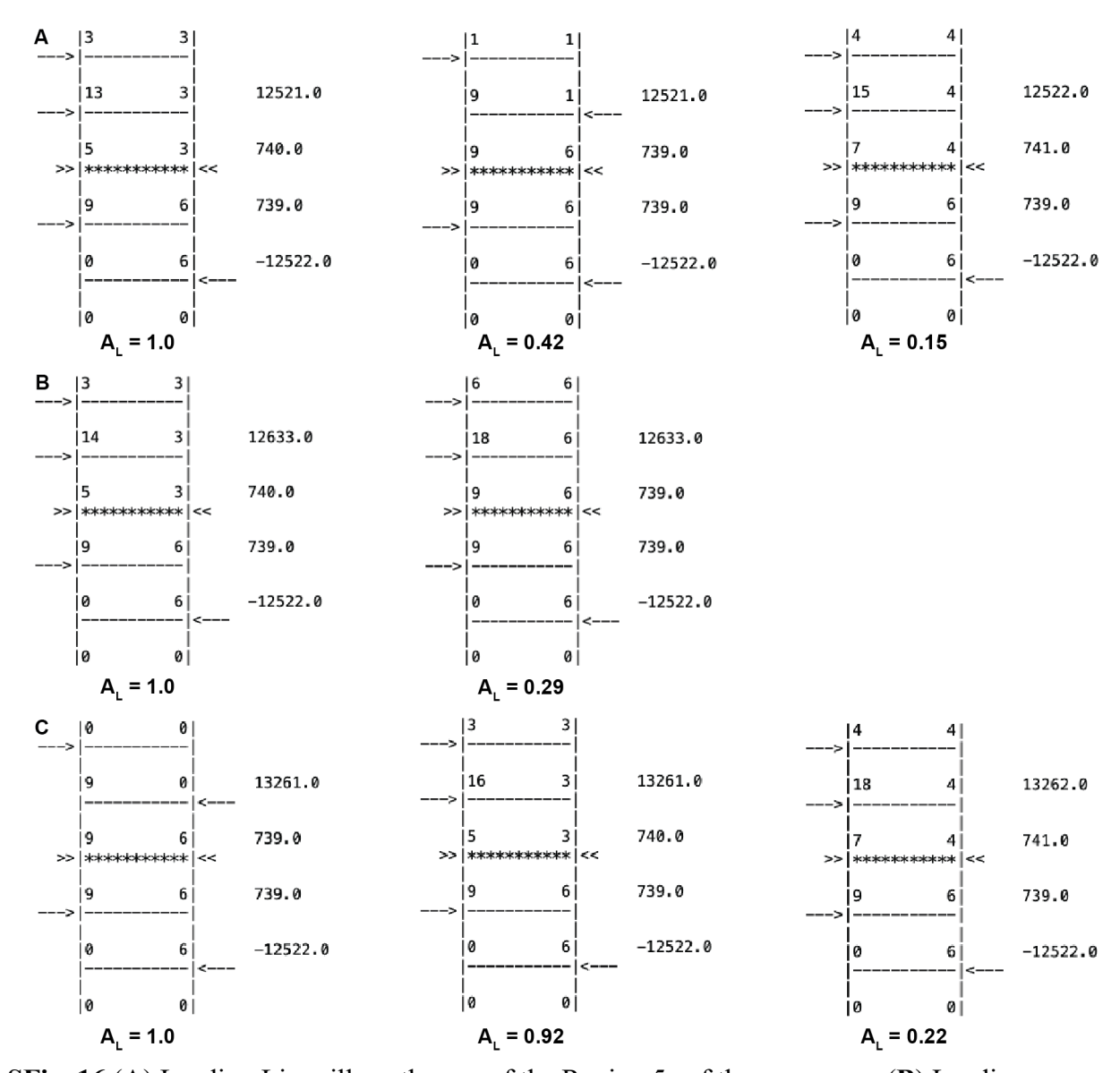




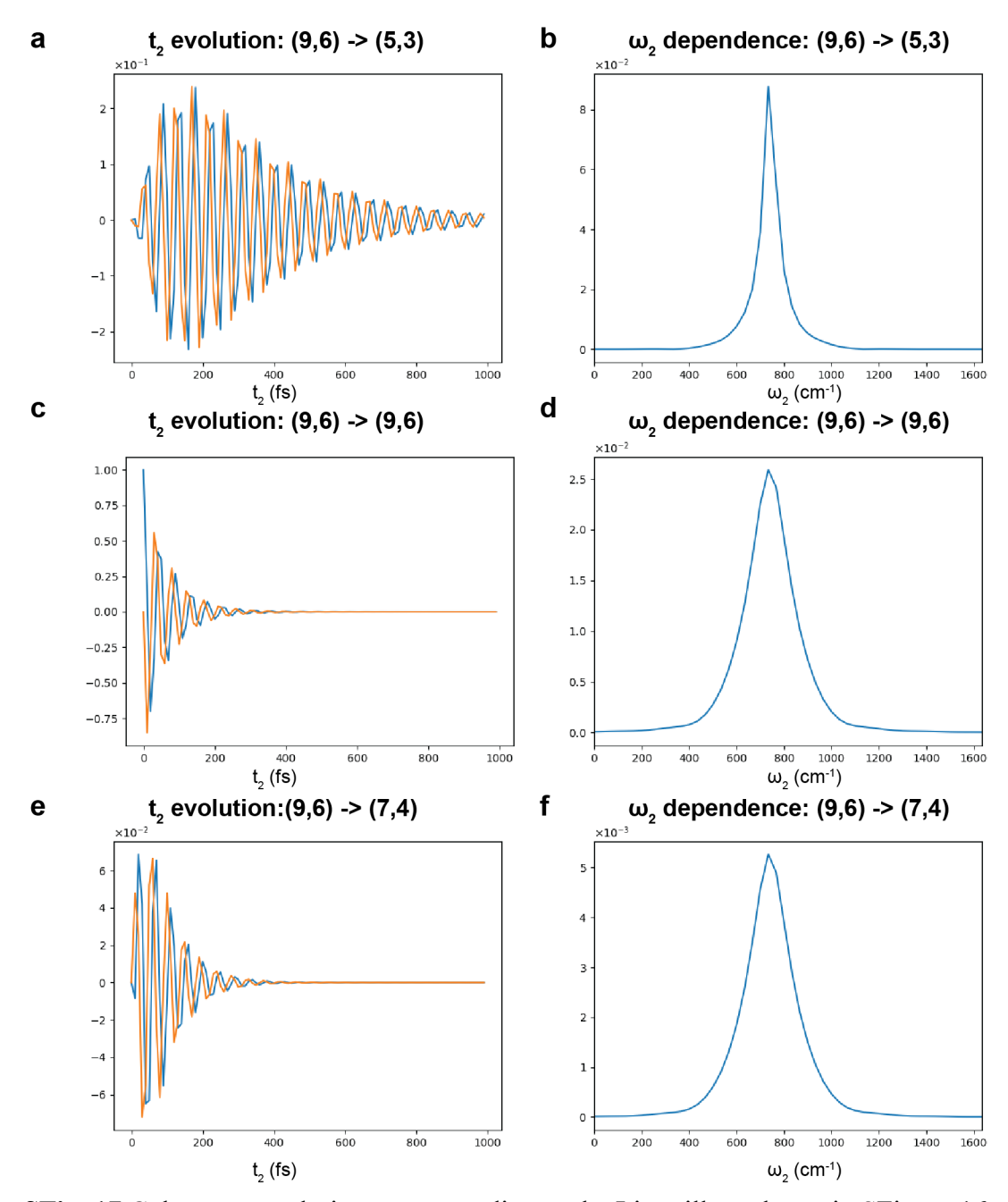
SFig. 14 (A)Leading Liouville pathways of the Region 1b of the ω_2 -map. (B) Leading Liouville pathways of the Region 2 of the ω_2 -map. An additional pathway with $A_L = 0.29$ exists with the excited state coherence (7,3) transferring to the coherence (5,3) and absorbing into state 16 just as the other two pathways which involve the (5,3) coherence. (C) Leading Liouville pathways of the Region 3 of the ω_2 -map. (D) Leading Liouville pathways of the Region 4 of the ω_2 -map.



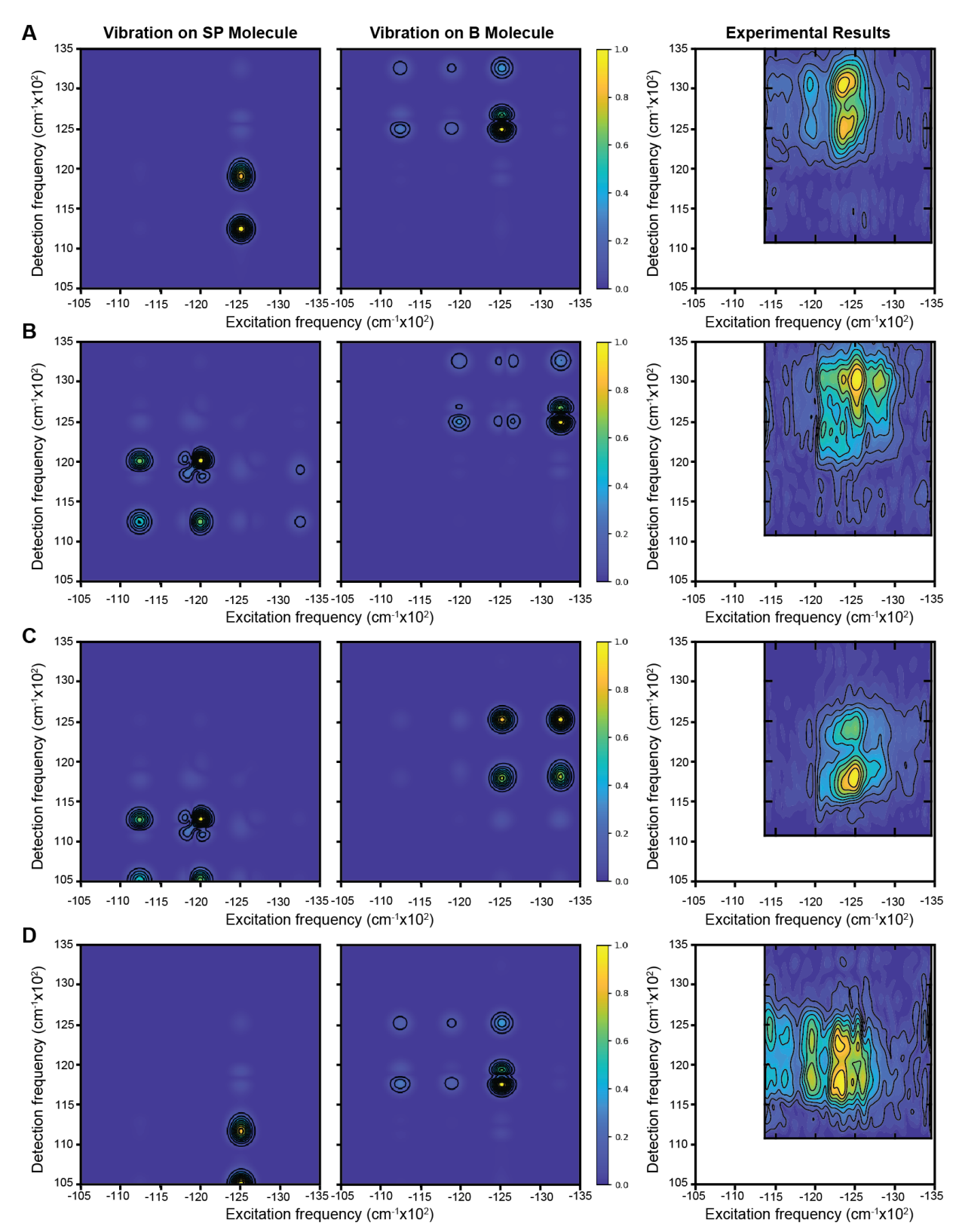
SFig. 15 Coherence evolution corresponding to the Liouville pathway in SFigure 14 and the corresponding Fourier transforms related to the strengths of the features in the 2D spectrum.



SFig. 16 (**A**) Leading Liouville pathways of the Region 5a of the ω_2 -map. (**B**) Leading Liouville pathways of the Region 5b of the ω_2 -map. (**C**) Leading Liouville pathways of the Region 6 of the ω_2 -map.



SFig. 17 Coherence evolution corresponding to the Liouville pathway in SFigure 16 and the corresponding Fourier transforms related to the strengths of the features in the 2D spectrum



SFig. 18 ω_2 -map theoretical simulation with vibrational mode placed on the SP molecule (left) and vibrational mode place on the B molecule (middle) compared with experimental results (right). (A) Rephasing ω_2 -map for positive frequency at $\omega_2 = 740$ cm⁻¹, (B) Rephasing

 ω_2 -map for negative frequency at $\omega_2 = 740$ cm⁻¹, (C) Non-rephasing ω_2 -map for positive frequency at $\omega_2 = 740$ cm⁻¹, (D) Non-rephasing ω_2 -map for negative frequency at $\omega_2 = 740$ cm⁻¹.

	Frequency [cm ⁻¹]	File name
Movie S1	570	SI_energy_gap_scan_om=570.mov
Movie S2	740	SI_energy_gap_scan_om=740.mov
Movie S3	900	SI_energy_gap_scan_om=900.mov

STable 1: Filenames of the mov movies representing real absolute value of the positive frequency rephasing ω_2 maps obtained in the energy gap ΔE scan between the values of **470** and **780** cm⁻¹. Other parameters of the model are presented in STable 2.

X	y	Z
0.7782	0.5332	0.3317
-0.9649	-0.02504	0.2613
0.854	0.5051	0.1206
	0.7782	0.7782 0.5332 -0.9649 -0.02504 0.854 0.5051 11575 12510 100 325 740 0.01 25

STable 2 Model parameters for simulation of the corresponds to the vibrational mode located on the B molecule of the BRC, and results in the spectrum of Figure 5.

Region	max ωexc (cm-1)	min ωexc (cm-1)	max ωdet (cm-1)	min ωdet (cm-1)
1a	11,000.0	11,500.0	12,000.0	12,600.0
1b	11,000.0	11,500.0	12,600.0	12,900.0
2	11,000.0	11,500.0	12,900.0	13,500.0
3	11,500.0	12,100.0	12,000.0	12,600.0
4	11,500.0	12,100.0	12,900.0	13,500.0
5a	12,100.0	13,000.0	12,000.0	12,600.0
5b	12,100.0	13,000.0	12,600.0	12,900.0
6	12,100.0	13,000.0	12,900.0	13,500.0

STable 3 Frequencies defining the studied regions of the ω_2 - maps. See Figure 5 for the location of the regions.

Exciton #	Approximate state composition
3	$ P_{-} angle B_{g0} angle$
4	$ P_{+}\rangle B_{g0}\rangle$
5	$ P_{-}\rangle B_{g1}\rangle$
6	$ B_{e0}\rangle$
7	$- P_{+}\rangle B_{g1}\rangle$
9	$ B_{e1}\rangle$
13	$ P_{-}\rangle B_{g0}\rangle$
14	$ 2SP\rangle B_{g1}\rangle$
15	$- P_{+}\rangle B_{e0}\rangle$
16	$ P_{-}\rangle B_{e1}\rangle$
18	$ P_{+}\rangle B_{e1}\rangle$

STable 4 Summary of exciton compositions (see SFig. 10 & 11 for further details).

Process during t_2	Local state basis	Process Type	Where found
$(5,3) \rightarrow (5,3)$	$(P_{-}B_{g1}, P_{-}B_{g0}) \rightarrow (P_{-}B_{g1}, P_{-}B_{g0})$	i (secular)	1a, 1b, 2
$(6,3) \rightarrow (5,3)$	$(B_{e0}, P B_{g0}) \rightarrow (P B_{g1}, P B_{g0})$	iii (nonsecular)	1a, 1b, 2
$(7,3) \Rightarrow (5,3)$	$(P_{+}B_{g1}, P_{-}B_{g0}) \rightarrow (P_{-}B_{g1}, P_{-}B_{g0})$	iv (nonsecular)	1a, 1b
(6,3) → (7,4)	$(B_{e0}, P B_{g0}) \rightarrow (P_+ B_{g1}, P_+ B_{g0})$	iii (nonsecular)	1a, 2
$(7,4) \to (5,3)$	$(P_+B_{g1}, P_+B_{g0}) \rightarrow (PB_{g1}, PB_{g0})$	iv (nonsecular)	3, 4
$(6,4) \rightarrow (5,3)$	$(B_{e0}, P_+ B_{g0}) \rightarrow (P B_{g1}, P B_{g0})$	iii (nonsecular)	3, 4
$(9,6) \to (9,6)$	$(B_{e1}, B_{e0}) \to (B_{e1}, B_{e0})$	i (secular)	5a, 5b, 6
$(9,6) \to (5,3)$	$(B_{e1}, B_{e0}) \rightarrow (P B_{g1}, P B_{g0})$	ii (nonsecular)	5a, 5b, 6
(9,6) → (7,4)	$(B_{e1}, B_{e0}) \rightarrow (P_+ B_{g1}, P_+ B_{g0})$	ii (nonsecular)	5a, 6

STable 5 Dominant coherence and coherence transfer processes observed during t_2 in exciton and local state bases. Also given are classifications of the process type and where the various processes appear on the ω_2 maps.

Science Advances Manuscript Template Page 68 of 70

Movie S1.

SI_energy_gap_scan_om=570.mov

Simulated real rephasing ω_2 -map for $\omega_2 = 570$ cm⁻¹, scanning the electronic energy gap ΔE through resonance.

SI_energy_gap_scan_om=740.mov

Simulated real rephasing ω_2 -map for $\omega_2 = 740$ cm⁻¹, scanning the electronic energy gap ΔE through resonance.

SI energy gap scan om=900.mov

Simulated real rephasing ω_2 -map for $\omega_2 = 900$ cm⁻¹, scanning the electronic energy gap ΔE through resonance.